Acta Geotechnica (2022) 17:4395–4418
https://doi.org/10.1007/s11440-021-01437-w

RESEARCH PAPER

Inspection of four advanced constitutive models for fine-grained soils under monotonic and cyclic loading

J. Duque[1] · M. Tafili[2] · G. Seidalinov[3] · D. Mašín[1] · W. Fuentes[4]

Received: 5 May 2021 / Accepted: 30 November 2021 / Published online: 19 March 2022

Abstract
A wide range of geotechnical structures founded in fine-grained soils are subjected to complex cyclic loading scenarios. The prediction of their behavior has motivated the development of several constitutive models for soils under different mathematical frameworks. Some success has been achieved under certain simplified cyclic conditions. However, the performance of the models is usually not satisfactory when dealing with a wide range of test conditions, such as variation of the loading amplitudes, initial effective stresses, initial stress ratios, overconsolidation ratios, direction of the loading with respect to the bedding plane, among others. Even though this issue is well-known by model developers, few efforts have been made in the literature to analyze and discuss this and other models' limitations. This article investigates the strengths and weaknesses of four advanced constitutive models for anisotropic fine-grained soils, namely: the anisotropic hypoplastic model by Fuentes et al. (Géotechnique 71(8):657–673, 2021), the SANICLAY-B elasto-plastic model by Seidalinov and Taiebat (Int J Numer Anal Meth Geomech 38(7):702–724, 2014), the constitutive Anamnesis model by Tafili (PhD thesis, Institute of Soil Mechanics and Rock Mechanics, Karlsruhe Institute of Technology, 2019) and the three surface kinematic hardening model proposed by Stallebrass and Taylor (Géotechnique 47(2):235–253, 1997) with transverse isotropic elasticity. In order to achieve that, simulation results with the models are qualitatively and quantitatively compared against a large number of experimental results under monotonic and cyclic loading on an anisotropic kaolin reported by Wichtmann and Triantafyllidis (Acta Geotech 13(5):1103–1128, 2018).

Keywords Boundary value problems · Constitutive modelling · Elastoplasticity · Hypoplasticity

1 Introduction

The study of cyclic loading on saturated clayey natural deposits is of high interest for the analysis of different geotechnical problems, as for example, offshore and onshore structures subjected to environmental loads, filling-emptying cycles on silos and water tanks, pavements under traffic loading, among many others [14, 17, 22, 45, 68]. Some particular characteristics observed on the cyclic behavior of natural clays take relevance on numerical predictions of these geotechnical problems, such as the accumulation rate of strains and pore water pressure [3, 7–10, 19, 26, 29, 38, 64], the stress attractors states in the sense of Gudehus [27, 28], the inherent and induced anisotropy [34, 35, 37, 59], among other observations. In particular, the material anisotropy affects the mechanical behavior depending on the angle between the loading direction and the bedding plane resulting from the material formation process [30, 51, 61, 63]. At large strain amplitudes, it leads to different strengths, stiffnesses and dilatancy-contractancy characteristics [16, 60, 67]. On the other hand, under small strain amplitudes, it affects the small strain stiffness [13, 18, 42, 48], the accumulation rates of strains and pore water pressure [1, 57, 61, 62, 67] and the inclination of the effective stress paths under undrained cyclic loading [56, 59, 68].

✉ J. Duque
duquefej@natur.cuni.cz

[1] Charles University, Prague, Czech Republic

[2] Ruhr-Universität Bochum, Bochum, Germany

[3] Fugro Germany Land GmbH, Berlin, Germany

[4] Pontificia Universidad Javeriana, Bogotá, Colombia

Reliable predictions of the aforementioned geotechnical problems dealing with water saturated fine-grained soils require robust constitutive models able to predict their behavior under undrained cyclic conditions. Their accuracy depends on their capabilities, which should include at least the above-mentioned observations. Authors of different models capable to reproduce monotonic and cyclic loading on fine-grained soils, have formulated models with different mathematical structures to allow the reproduction of some anisotropic effects. It is difficult to classify models for cyclic loading in fine-grained soils, but some key ingredients considered in their formulation provide some hints about their capabilities and limitations. For example, it is expected that models including Cam-Clay type yield surfaces, able to harden kinematically, are capable to simulate the influence of anisotropy on the stiffness and strength, but cannot provide different small strain stiffnesses depending on the bedding plane orientation. On the other hand, models accounting for anisotropic elastic tensors, do consider the dependence of small strain stiffness with the bedding plane orientation, but do not guarantee correct assessment on cycles close to the critical state, where fabric changes due to large deformations are important. Some recent constitutive models, e.g. [32, 46, 69] have accounted for anisotropic effects by considering a fabric tensor and the anisotropic critical state theory by Li and Dafalias [31]. Finally, the prediction of the accumulation rate of strains and pore water pressure, which is known to depend on the loading direction, depends on the special features of the plastic strain rate formulation.

Contrasting with many works in the literature, the present one aims to show and analyze the main advantages and limitations of some available constitutive models, claiming to reproduce the monotonic and cyclic behavior of anisotropic fine-grained soils. This is achieved by analyzing the simulations with four different models for cyclic loading for anisotropic fine-grained soils, basing their formulations on different mathematical structures, namely: the anisotropic hypoplastic model extended with Intergranular Strain Anisotropy (AHP+ISA) by Fuentes et al. [18], the SANICLAY-B elasto-plastic model by Seidalinov and Taiebat [53], the Anamnesis model by Tafili [56] and the three surface kinematic hardening model by Stallebrass and Taylor [55], adopting the well-known relations for transverse isotropic elasticity by Graham and Houlsby [25]. Simulations will be performed and compared with monotonic and cyclic tests on an anisotropic kaolin reported by Wichtmann and Triantafyllidis [68]. The experiments include an oedometer test with multiple unloading-reloading cycles, five undrained monotonic triaxial tests and sixteen undrained cyclic triaxial tests with different controls and initial conditions on samples having vertical and horizontal cutting directions.

The structure of the paper is as follows: First, the main characteristics of each inspected constitutive model are given. Then, a brief description of the numerical implementations is presented. Subsequently, the testing material and selected experiments for simulation purposes are described. After that, the performance of the models is evaluated through the comparison between experimental results and element test simulations. At the end, the weaknesses and strengths of each model are remarked. The notation and convention is as follows: scalar magnitudes (e.g. a, b) are denoted by italic fonts, vectors (e.g. $\mathbf{a}, \mathbf{b}$) with bold lowercase fonts, second-rank tensors (e.g. $\mathbf{A}$, $\mathbf{B}$) with bold capital letter or bold symbols, higher ranked tensors with special fonts (e.g. E, L). Components of the tensors are denoted through indicial notation (e.g. A_{ij}). The Kronecker delta is represented with $1_{ij} = \delta_{ij}$. Components of the effective stress tensor $\boldsymbol{\sigma}$ or strain tensor $\boldsymbol{\varepsilon}$ in compression are negative. In the triaxial space, Roscoe's invariants are defined as $p = (\sigma_a + 2\sigma_r)/3$, $q = (\sigma_a - \sigma_r)$ and $\varepsilon_v = (\varepsilon_a + 2\varepsilon_r)$, $\varepsilon_q = 2(\varepsilon_a - \varepsilon_r)/3$, respectively. The subscripts a and r denote the axial and radial directions, respectively. The stress ratio η is defined as $\eta = q/p$.

2 Brief description of the constitutive models

In this section, four existing constitutive models able to describe the behavior of anisotropic clays under monotonic and cyclic loading are briefly explained. We begin with the anisotropic hypoplastic model for clays by Fuentes et al. [18], hereafter referred as AHP+ISA. Its formulation is basically based on extending the anisotropic hypoplastic model for clays by Mašín [34], with the Intergranular Strain Anisotropy (ISA) approach by Fuentes and Triantafyllidis [21]. The resulting model presents some important features compared to the former version by Mašín [34], such as the reduction of overshooting effects and improved capabilities on the reproduction of pore water pressure under undrained cyclic loading. It also incorporates a transversely isotropic stiffness tensor to account for anisotropic effects on the small strain behavior. Its calibration requires a number of 15 parameters, which are listed in Table 1.

The SANICLAY-B is an anisotropic critical state model proposed by Seidalinov and Taiebat [52, 53]. This model corresponds to an improved version of the SANICLAY model by Dafalias et al. [11] with the following characteristics: it accounts for a new bounding surface formulation based on a proper repositioning mechanism of the

Table 1 Parameters of the AHP+ISA model for kaolin

φ_c [°]	ξ [-]	λ^* [-]	κ^* [-]	N [-]	ν [-]	α_G [-]	A_g [-]	n_g [-]	R [-]	β_{h0} [-]	β_{hmax} [-]	χ_0 [-]	χ_{max} [-]	C_a [-]
26	5.7	0.087	0.013	1.215	0.35	1.9	135	1	0.00035	0.42	1.2	4.3	17	0.018

projection center in order to improve cyclic loading simulations. In addition, it considers a damage parameter to describe the stiffness degradation upon cyclic mobility effects. Mechanisms describing the isotropic and rotational hardening as well as the elastic behavior are similar to the ones proposed by Dafalias et al. [11]. The resulting model presents in general improved capabilities on the reproduction of undrained cyclic loading and cyclic mobility effects. It requires 11 parameters which are presented in Table 2.

The recently proposed Anamnesis model by Tafili [56], hereafter denoted as CAM, is also analyzed in the present work due to the following features. Its formulation incorporates a transversal hypoelastic stiffness tensor to consider anisotropic small strain effects. For this purpose, the existent hypoelastic stiffness is transformed (rotated and scaled) after defining the bedding plane orientation. The strain rate is decomposed into a hypoplastic and a time-dependent one. The hypoplastic strain rate accounts for induced anisotropic effects by considering a back-stress type tensor while the viscous strain rate considers a similar formulation to the ISA-Clay model by [20]. In general, the model incorporated a yield surface, the so-called historiotropic surface, through which the model can be classified also as elastoplastic. Hence, the mathematical formulation of CAM combines the two pioneer developments - hypoplasticity and elastoplasticity. This novel formulation is able to reproduce fairly well the stress-strain behavior of anisotropic clays under cyclic loading, including some viscous effects such as creep and stress relaxation. The model accounts for 15 parameters which are presented in Table 3.

An extended version of the three surface kinematic hardening model proposed by Stallebrass and Taylor [55] is herein considered and analyzed. The extended model, hereafter denoted as the A3-SKH model, results from adopting the well-known relations for transverse isotropic elasticity by Graham and Houlsby [25]. The A3-SKH model incorporates a bounding surface describing the limit of all admissible stress state, and includes two kinematic surfaces, corresponding to the yield and history surfaces, with similar (but not equal) formulations and hardening mechanisms to the ones proposed by Al Tabbaa and Wood [2]. The three surfaces share the same geometrical shape (elliptical), but different sizes. The A3-SKH model consists of 11 parameters which are presented in Table 4.

Table 2 Parameters of the SANICLAY-B model for kaolin

M_c [−]	M_e [-]	λ [-]	κ [-]	ν [-]	N [-]	h_0 [-]	a_d [-]	C [-]	x [-]	k_i [-]
0.9	0.84	0.17	0.01	0.2	0.93	50	3	3	1.64	0

It is worthy to remark, that the calibration procedure of the model's parameters was performed by its corresponding model developer, to achieve their best performance. It is, however, important to point out that two of the models analyzed (AHP+ISA and CAM models) have been developed using the same or similar data as used for model evaluation in this paper, they have thus been developed for best performance using this dataset. The other two models (SANICLAY-B and A3-SKH) have been developed using different data: SANICLAY-B focusing on larger amplitude cyclic tests and A3-SKH focusing on directional small-strain stiffness predictions.

Numerical implementations of the CAM and AHP+ISA models considered a substepping explicit scheme, with very small strain increments to provide numerical convergence. They were written using FORTRAN following the "UMAT" syntax from the commercial software ABAQUS Standard. Element test simulations with the CAM and AHP+ISA models were performed with the software INCREMENTAL DRIVER by Niemunis [41]. On the other hand, element test simulations with the SANICLAY-B model were performed using the nonlinear finite-difference code Fast Lagrangian Analysis of Continua (FLAC), while a Forward-Euler scheme was employed for the A3-SKH model. The element test simulations with the A3-SKH model were performed with the element test driver TRIAX developed by Mašín [36].

3 Test material and experiments

Experimental results on the anisotropic kaolin reported by Wichtmann and Triantafyllidis [68] are used to analyze the models capabilities. This kaolin has been found to present an anisotropic microstructure arrangement according to some previous studies using scanning electron microscope (SEM) [23]. It is classified as a low plasticity silt (ML), see

Table 3 Parameters of the CAM model for kaolin

φ_c [°]	λ [−]	κ [−]	e_{i0} [−]	v_h [−]	α [−]	I_v [−]	n_{peak} [−]	n_{ptl} [−]	n_o [−]	n_{oi} [−]	c_B [−]	C_2 [−]	$n_{Y,D0}$ [−]	β_d [−]
26	0.055	0.03	1.158	0.3	1.7	0.02	5.5	8	15	2	0.5	30	0.8	2

Table 4 Parameters of the A3-SKH model for kaolin

φ_c [°]	λ^* [-]	κ^* [-]	N [-]	A_g [-]	n_g [-]	m [-]	α [-]	T [-]	S [-]	ψ [-]
26	0.087	0.013	1.215	135	1	0.2	1.9	0.25	0.08	2.1

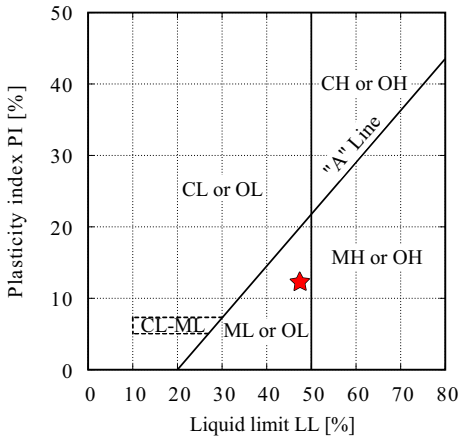

Fig. 1 Position of the kaolin in the Casagrande plasticity diagram

Fig. 1, and presents the following characteristics: specific gravity of $G_s = 2.675$, liquid limit of $LL = 47.2\%$, plastic limit of $PL = 35.0\%$, and plasticity index of $PI = 12.2\%$. Samples were prepared by mixing a kaolin dry powder with demineralized water with an initial water content $w_i = 2.5\,LL$. Then, samples were pre-consolidated with a maximum vertical stress of $\sigma_1 = 100$ kPa. In order to inspect its anisotropic properties, cylindrical samples with dimensions $d = h = 50$ mm (diameter and height, respectively) were cut out and tested considering different bedding plane's orientation in the following way: "vertical samples" were cut out vertically and present horizontal bedding plane, while "horizontal samples" were cut out horizontally and present vertical bedding plane, see Fig. 2. For a more detailed description of the experimental procedure, readers are referred to [68].

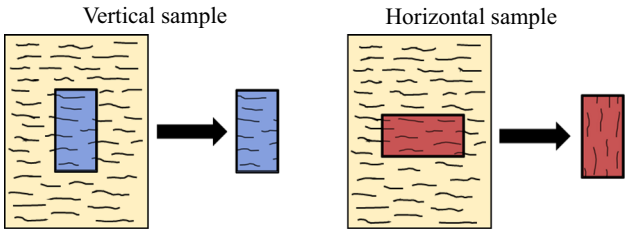

Fig. 2 Schematic cutting direction of samples

Table 5 summarizes the testing program reported in [68] and used in the present work. An oedometric compression test with three unloading-reloading cycles, five undrained monotonic triaxial tests and sixteen undrained cyclic triaxial tests are considered. The undrained monotonic triaxial tests were performed on normally consolidated samples considering different initial mean effective pressures $p_0 = \{50, 100, 200, 300, 400\}$ kPa. The first series of the undrained cyclic triaxial tests consist of six tests with different deviatoric stress amplitudes $q^{\text{amp}} = \{30, 40, 45, 50, 60, 70\}$ kPa and isotropic initial stress of $p_0 = 200$ kPa. The testing program under undrained cyclic loading also includes the following variations: four tests with anisotropic initial stresses $\eta_0 = q_0/p_0 = \{0.25, 0.125, -0.125, -0.25\}$ and $p_0 = 200$ kPa; three tests with different initial overconsolidation ratios $\text{OCR} = \{1.5, 2.0, 2.5\}$ and two tests controlled with axial strain cycles and different axial strain amplitudes $\varepsilon_1^{\text{amp}} = \{1, 2\}$ %. Finally, a sample with vertical bedding plane (cut out in the horizontal direction) with $p_0 = 200$ kPa subjected to undrained deviatoric cyclic loading with $q^{\text{amp}} = 45$ kPa is considered.

Table 5 includes the number of simulated cycles by the models N_s and the number of cycles to reach $|\varepsilon_1| = 10\%$ in the experiments N_f. The authors decided to limit their simulations to a maximum number of $N_s = 150$ considering that numerical errors resulting from the integration of incremental-based models are accumulated upon increasing number of cycles [39, 40, 66, 67]. To avoid this issue, models depending explicitly on the number of cycles, e.g. [6, 24, 33, 44, 49, 67], are a more appropriate approach when $N_s > 150$. For the particular case of the SANICLAY-B model, some simulations were stopped before 150 cycles due to the fact that the model produced excessive accumulation of strains for larger number of cycles, as it was developed for earthquake applications where smaller number of cycles are expected.

Table 5 Testing program with the kaolin reported by Wichtmann and Triantafyllidis [68]

Test name	p_0 [kPa]	q_0 [kPa]	q^{amp} [kPa]	ε_1^{amp} [%]	N_s [-]	N_f [-]	OCR [-]	e_0 [-]	Cutting direction
O1*	–	–	–	–	–	–	–	1.424	Vertical
M1†	50	0	–	–	–	–	1.33	1.434	Vertical
M2†	100	0	–	–	–	–	1.00	1.332	Vertical
M3†	200	0	–	–	–	–	1.00	1.332	Vertical
M4†	300	0	–	–	–	–	1.00	1.244	Vertical
M5†	400	0	–	–	–	-	1.00	1.214	Vertical
C1‡	200	0	30	–	150	>4368	1.00	1.250	Vertical
C2‡	200	0	40	–	150	492	1.00	1.147	Vertical
C4‡	200	0	45	–	131	131	1.00	1.193	Vertical
C5‡	200	0	50	–	68	68	1.00	1.145	Vertical
C7‡	200	0	60	–	11	11	1.00	1.202	Vertical
C8‡	200	0	70	–	7	7	1.00	1.121	Vertical
C26‡	200	50	30	–	150	319	1.00	1.249	Vertical
C27‡	200	25	30	–	150	>2272	1.00	1.319	Vertical
C28‡	200	-25	30	–	150	>7286	1.00	1.248	Vertical
C29‡	200	-50	30	–	150	>2418	1.00	1.248	Vertical
C37‡	100	0	30	–	115	115	1.50	1.239	Vertical
C38‡	100	0	30	–	115	531	2.00	1.200	Vertical
C39‡	100	0	30	–	115	904	2.50	1.146	Vertical
C41‡	200	0	45	–	150	614	1.00	1.252	Horizontal
C43‡	300	0	–	1	150	–	1.00	1.046	Vertical
C44‡	300	0	–	2	150	–	1.00	1.057	Vertical

* Oedometric compression test

† Undrained monotonic triaxial test

‡ Undrained cyclic triaxial test

4 Element test simulations with the inspected models

The experimental tests listed in Table 5 are now used for simulation purposes. For the simulations, the preloading consolidation history was always reproduced (i.e. isotropic consolidation or isotropic with subsequent anisotropic consolidation). Appendix 7.2 provides detailed information related to the initialization of the state variables, and the reproduced preloading consolidation paths.

4.1 Oedometric compression and monotonic triaxial tests

Simulations of the oedometric test O1 (see Table 5), which includes three unloading-reloading cycles and some creep stages (see test description in [20]), is in the following analyzed. The experimental path is compared to simulations in Fig. 3. It is recalled, that the only model able to capture the time-dependent behavior, such as creep, is the CAM model, as shown in Fig. 3a. This is attributed to the incorporation of a viscous strain rate and a proper calibration of the viscous parameter I_v. Stiffness characteristics at medium and large strains were also well reproduced by the CAM model, while an underestimation on the stiffness is observed at the beginning of each reloading path, see Fig. 3a. This suggests that the reproduction of small strain effects should be revised in the CAM model. On the contrary, the AHP+ISA model successfully reproduced the first loading path, as well as the hysteresis upon the unloading/reloading path, due the consideration of small strain effects, see Fig. 3b. Simulation results with the SANICLAY-B and A3-SKH models are presented in Fig. 3c,d. showing both a similar pattern: upon the first

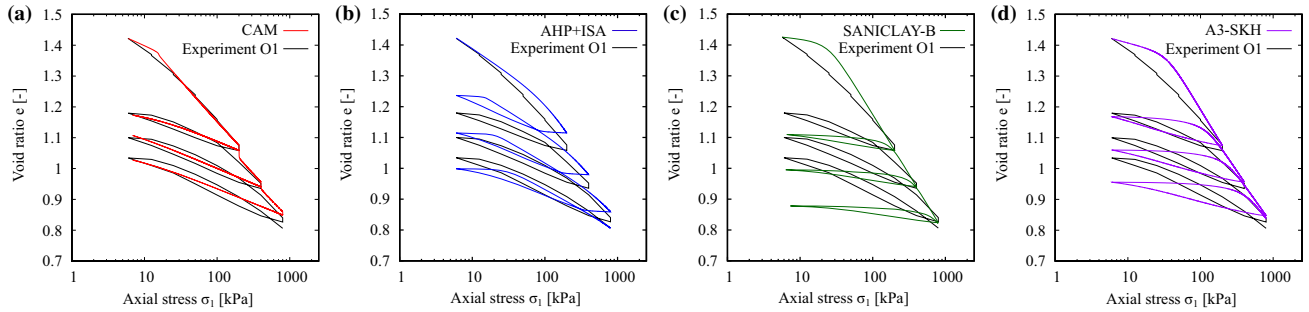

Fig. 3 Simulations of the oedometric test O1 with three unloading-reloading cycles, $e - \sigma_1$ space: **a** CAM, **b** AHP+ISA, **c** SANICLAY-B, **d**A3-SKH

loading path, both reproduced a stiffer behavior before reaching the normal consolidation line. Regarding to the unloading-reloading path, they both managed to reproduce satisfactorily a hysteretic effect, while the overall secant stiffness is overestimated. The latter issue is related to the fact that their parameters controlling the unloading stiffness were calibrated to provide their best performance on the undrained cyclic triaxial tests, and not on the oedometric cycles. Overshooting effects, usually observed after unloading-reloading paths in many models for cyclic loading, such as in the conventional intergranular strain model by Niemunis and Herle [43] and the hardening soil model by Schanz et al. [50], extended with small strain stiffness according to Benz et al. [4, 5], were not found in these particular simulations.

Simulations of five undrained monotonic triaxial tests (see M1-M5 in Table 5) on normally consolidated samples with different initial mean effective pressures $p_0 = \{50, 100, 200, 300, 400\}$ kPa were performed for calibration purposes. They in general show an agreement with the experiments, however, a few observations are worthy to remark: the experiments show that the peak is reached at large deformations $\varepsilon_1 > 10\%$. This behavior was only well captured by the CAM model and the A3-SKH model, since they consider hardening mechanisms which are still active upon medium and large strains. In contrast, the AHP+ISA and SANICLAY-B reached a peak behavior at lower strains since they lack of the aforementioned mechanisms. Instead, these models rendered an almost constant deviatoric stress after failure conditions were reached. This effect is much more pronounced on the SANICLAY-B model due to its stiffer response, since parameters controlling the small strain stiffness were selected with special focus to reproduce the undrained cyclic loading and not the monotonic loading (Fig. 4).

4.2 Undrained cyclic triaxial tests

In the present section, constitutive models are now inspected under undrained cyclic loading. Variation of the deviatoric stress amplitude, initial stress ratio, overconsolidation ratio, axial strain amplitude, and finally, cutting direction (and therefore its bedding plane orientation) are considered.

4.2.1 Variation of deviatoric stress amplitude

In the following, simulations of undrained cyclic triaxial tests on normally consolidated samples after isotropic consolidation ($p_0 = 200$ kPa, $q_0 = 0$) considering different deviatoric stress amplitudes $q^{\text{amp}} = \{30, 40, 45, 50, 60, 70\}$ kPa are carefully analyzed. The experimental results as well as their respective simulations in the $q - p$ space are presented in Fig. 5. From the plots, one immediately notes, that the liquefaction state $p = q = 0$ is not reached in any experiment. Instead, cycles close to the critical state line exhibit "eight-shaped" effective stress loops accompanied with the development of large strain amplitudes. This "eight-shaped" effective stress loops were only predicted by the CAM model, attributed to the consideration of an interaction between inherent anisotropy and dilatancy of the material on its flow rule formulation.

The experiments suggest that the pore water pressure accumulation rate, and therefore the number of cycles to reach the failure criterion (e.g. $|\varepsilon_1| = 10\%$), strongly depends on the magnitude of the deviatoric stress amplitude. On one hand, it is noted that test C1 presenting the lowest deviatoric stress amplitude ($q^{\text{amp}} = 30$ kPa) did not reach $|\varepsilon_1| = 10\%$ after a number of $N = 4368$ cycles. On the other hand, test C8 presenting the highest deviatoric stress amplitude ($q^{\text{amp}} = 70$ kPa) reached the failure criterion $|\varepsilon_1| = 10\%$ after only 7 cycles. From the simulations, one may conclude the following: the CAM model predicts well the mean effective stress reduction upon the cycles under different deviatoric stress amplitudes, see Fig. 5e–h. This is attributed to the rotation mechanism of the historiotropic flow surface, which affects directly the hypoplastic volumetric strain rate and thus the pore pressure accumulation rate. The AHP+ISA model was able to reproduce accurately the variation of the mean effective

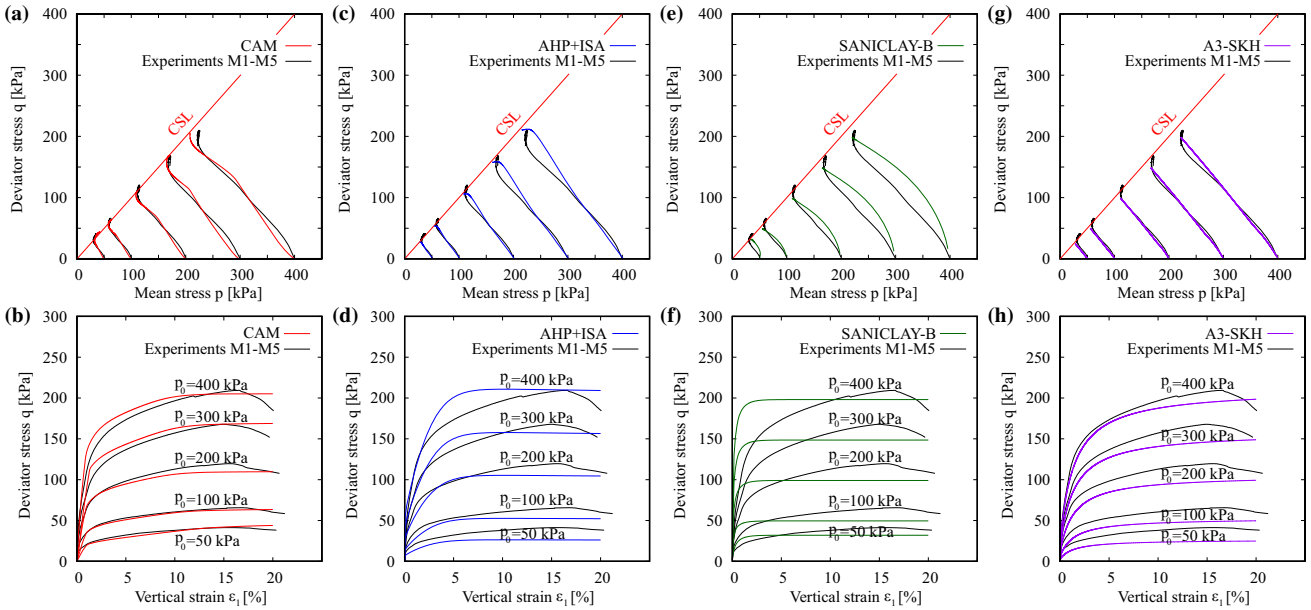

Fig. 4 Simulations of undrained monotonic triaxial tests M1-M5 on normally consolidated samples with isotropic consolidation ($q_0 = 0$, $\eta_0 = 0$) and variation of the initial mean effective pressures $p_0 = \{50, 100, 200, 300, 400\}$ kPa: **a**, **b** CAM, **c**, **d** AHP+ISA, **e**, **f** SANICLAY-B, **g**, **h** A3-SKH

stress accumulation rate, see Fig. 5i–l. This behavior was achieved due to the evolution of function χ, controlling directly the accumulation rate, which increases its value from parameters χ_0 to χ_{max} upon increasing number of cycles. Pore water pressure generation of the critical state-based elasto plastic models (SANICLAY-B and A3-SKH models) is controlled by the adopted plastic potentials, such that compressive plastic volumetric strain rate imply positive pore water pressure generation and dilative plastic volumetric strain rate imply negative pore water pressure generation if undrained (constant volume) conditions are imposed. As a matter of fact, due to the adopted model structure defined by kinematic hardening (for A3-SKH) and mapping rules (for SANICLAY-B), these models predict negligible plastic volumetric strains not only at the critical state defined by mean effective stress, void ratio and stress ratio, but even if stress ratio is lower than the one corresponding to critical state. Therefore, pore water pressure accumulation stops as soon as mean effective stress reaches critical state value (for current void ratio). This behavior limits the applicability of these models on problems with cyclic loading, whereby the accumulation of excess pore water pressure is essential.

The effective stress paths show a remarked inclination in the $q - p$ space caused by the material's inherent anisotropy. This effect was successfully captured by the CAM and AHP+ISA models, due to the incorporation of a bedding plane-dependent hypoelastic stiffness. It should be mentioned, that these parameters were calibrated to reproduce satisfactorily the small shear stiffness anisotropy, and not the resulting inclination of the effective stress paths on undrained elastic cycles. Therefore, this inclination is considered as a model prediction. While the CAM model incorporates the parameter α to simulate the material's anisotropy, the AHP+ISA model employs parameter α_G for the same purpose. The SANICLAY-B model was not able to reproduce the inclination of the effective stress paths since it considers isotropic (hypo-)elasticity. On the other hand, the A3-SKH model incorporates a transversely isotropic hypoelastic stiffness, but it is evident that the observed effective stress paths inclination does not coincide with the experiments because only the elastic part of the model accounts for inherent anisotropy, and the elastic range of the model is very small. Therefore, the overall response of the model is governed by the elastic and plastic components.

The experimental results in stress-strain space are presented in Fig. 6a–d. They suggest that the vertical strain accumulation runs at a slow rate until reaching cyclic mobility, in which the double strain amplitude quickly grows with each subsequent cycle. Simulation results with the CAM model suggest that the accumulation of vertical strains before the mobilized cycles was particularly well predicted. The amplitude and shape of the stress-strain hysteresis at cyclic mobility are accurately described, however, the model accumulates in extension despite the accumulation of the experiments in compression. On the other hand, the AHP+ISA predicts a bias in strain accumulation on the compression side after reaching the last mobilized cycles. This behavior is associated with the

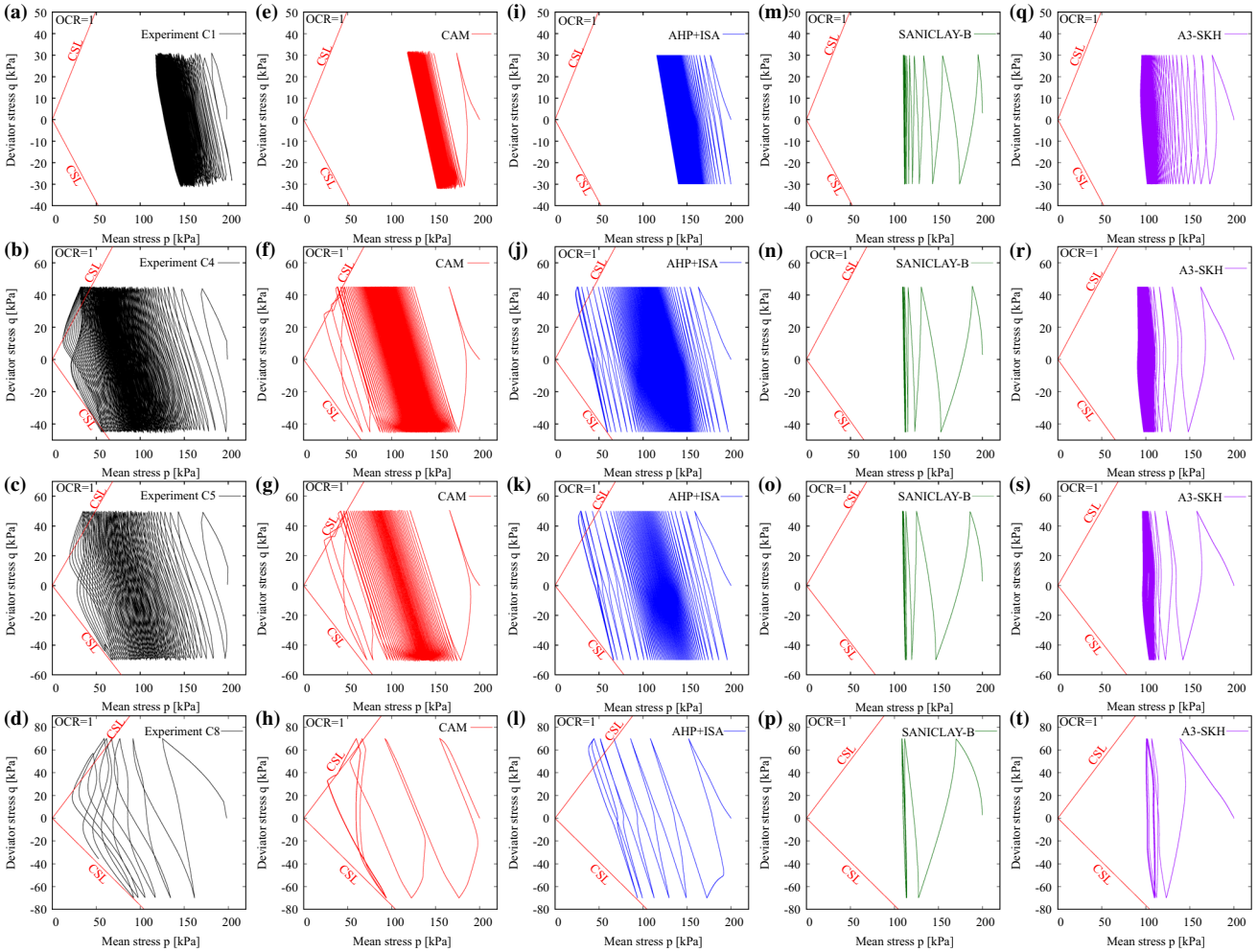

Fig. 5 Simulations of undrained cyclic triaxial tests C1-C8 on normally consolidated samples with isotropic consolidation ($p_0 = 200$ kPa, $q_0 = 0$, $\eta_0 = 0$) and variation of the deviatoric stress amplitude $q^{amp} = \{30, 45, 50, 70\}$ kPa, $q - p$ space: **a–d** experiments by Wichtmann and Triantafyllidis [68], **e–h** CAM, **i–l** AHP+ISA, **m–p** SANICLAY-B, **q–t** A3-SKH

effect of the Lode's angle on the critical state surface (with different compression and extension critical state slopes). The bias in strain accumulation after cyclic mobility is actually a common limitation of most hypoplastic models and remarks the need to reformulate the dilatancy-contractancy changes at large strain amplitudes (due to the rearrangement of the particles) and the stiffness degradation of most of these type of models [12, 15, 56]. This issue limits the capabilities of the model on problems where the behavior at large deformations take relevance, such as analysis under seismic conditions with a number of cycles. Recent constitutive models for sands, e.g. [32, 46, 69] have properly addressed these issues by considering the anisotropic critical state theory by Li and Dafalias [31] and an adequate definition of the fabric influence on dilatancy. Simulation results with the SANICLAY-B model are presented in Fig. 6m–p and suggest that this is the only model which realistically reproduces the accumulation of vertical strains both before and after cyclic mobility. Finally, simulations results with the A3-SKH model suggest that the model does not present a bias in strain accumulation, but fails to reproduce the increasing magnitude of the axial strain in double amplitude with each subsequent cycle.

The analysis of the accumulated pore water pressure p_w, computed at the middle of each cycle, is presented in Fig. 7. The results suggest that the CAM and AHP+ISA models were able to reproduce the strong dependency of the pore water pressure accumulation on the deviatoric stress amplitude q^{amp}. On the other hand, the SANICLAY-B and A3-SKH models reproduced a similar pore water pressure accumulation independently of the deviatoric stress amplitude. The proper reproduction of the pore water pressure accumulation with different deviatoric stress amplitudes is a complex task from the constitutive description point of view. Wichtmann [67] reported that even advanced models as the anisotropic visco-hypoplastic

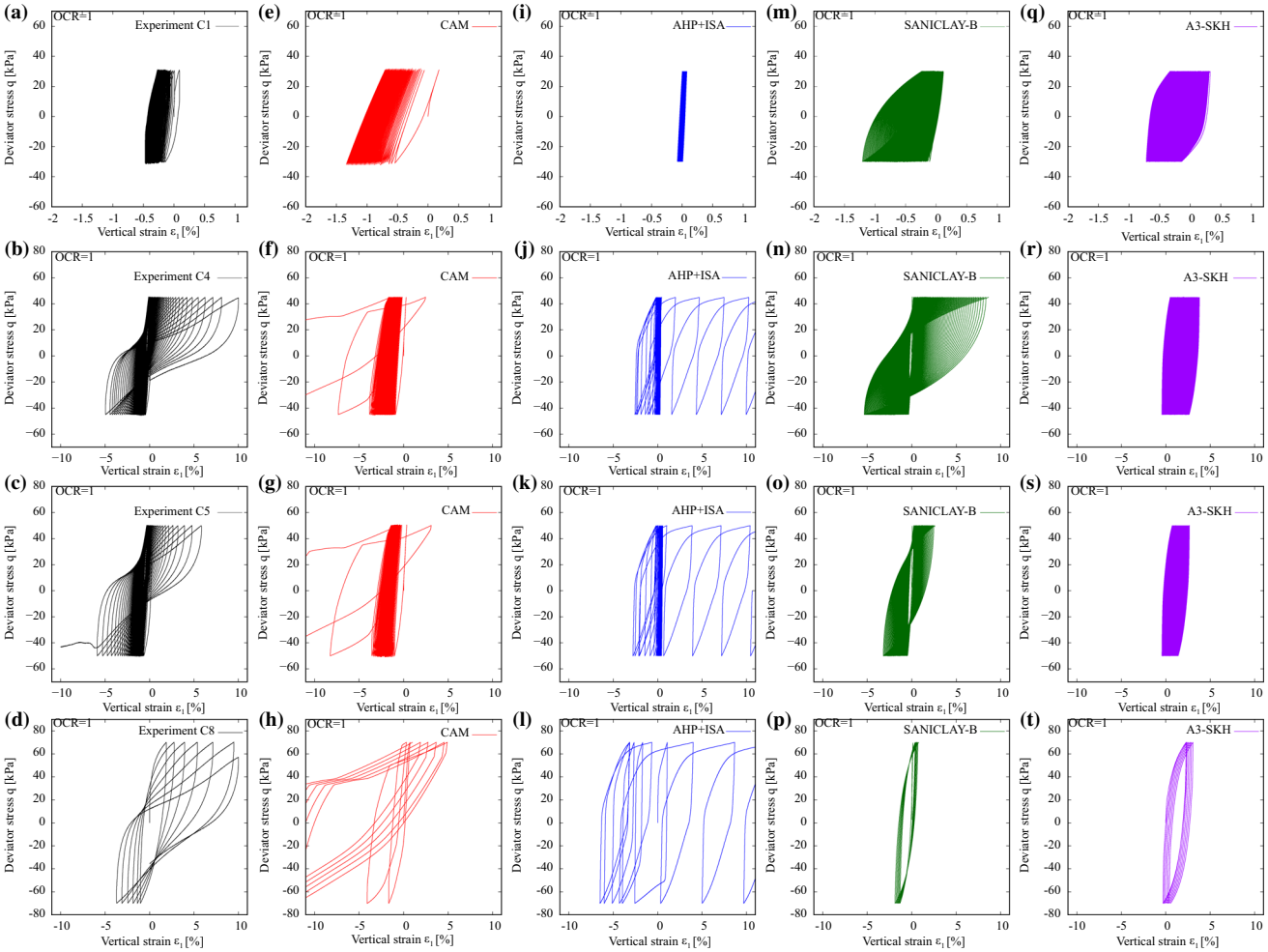

Fig. 6 Simulations of undrained cyclic triaxial tests C1-C8 on normally consolidated samples with isotropic consolidation ($p_0 = 200$ kPa, $q_0 = 0$, $\eta_0 = 0$) and variation of the deviatoric stress amplitude $q^{\text{amp}} = \{30, 45, 50, 70\}$ kPa, $q - \varepsilon_1$ space: **a–d** experiments by Wichtmann and Triantafyllidis [68], **e–h** CAM, **i–l** AHP+ISA, **m–p** SANICLAY-B, **q–t** A3-SKH

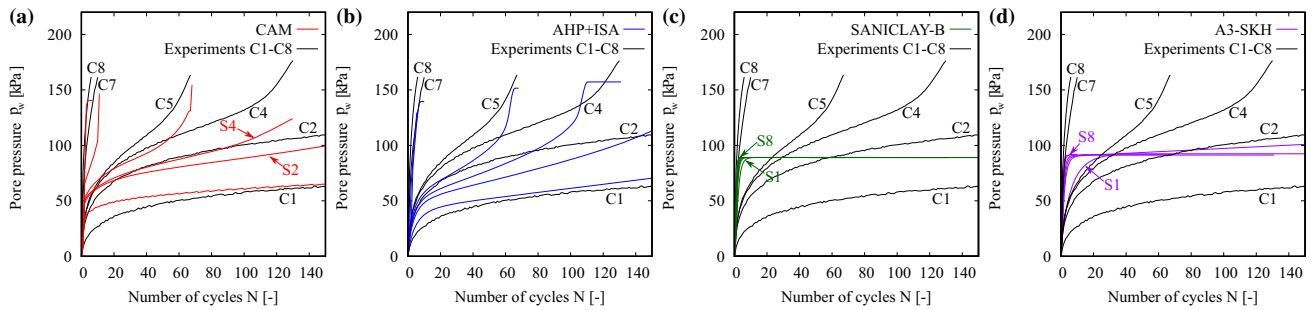

Fig. 7 Simulations of the accumulated pore water pressure in undrained cyclic triaxial tests C1-C8 on normally consolidated samples with isotropic consolidation ($p_0 = 200$ kPa, $q_0 = 0$, $\eta_0 = 0$) and variation of the deviatoric stress amplitude $q^{\text{amp}} = \{30, 40, 45, 50, 60, 70\}$ kPa: **a** CAM, **b** AHP+ISA, **c** SANICLAY-B, **d** A3-SKH

model for clays by Niemunis et al. [42], have problems to accurately reproduce a wide range of cyclic conditions with a single set of parameters.

In order to analyze the number of cycles to reach the state at which large strain amplitudes are developed, two failure criteria are hereafter considered: a) axial strain in single amplitude of $\varepsilon_1^{\text{SA}} = 10\%$, and b) axial strain in double amplitude of $\varepsilon_1^{\text{DA}} = 10\%$, see Fig. 8a,b. The analysis of the cyclic stress ratio $\text{CSR} = q^{\text{amp}}/(2p_0)$ against the number of cycles to reach failure N_{f} is presented in

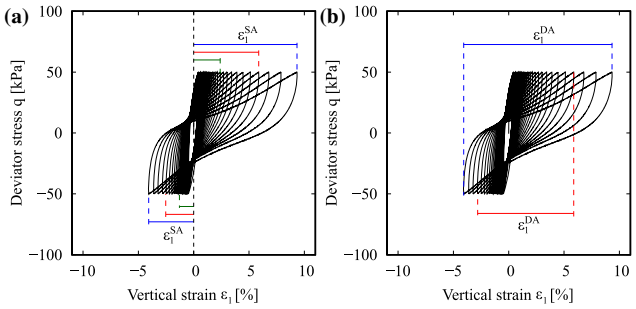

Fig. 8 Description of the selected failure criteria: **a** $\varepsilon_1^{SA} = 10\%$, **b** $\varepsilon_1^{DA} = 10\%$

Fig. 9. For the construction of the experimental curves, the results of tests C1-C8 (with variation of q^{amp} and $p_0 = 200$ kPa) were considered and are presented as black triangles. In addition, a potential fitting regression was also included as a continuous solid black line. Simulations with the CAM model suggest an accurate performance for both failure criteria. On the other hand, the AHP+ISA model was only able to reach the failure criterion $\varepsilon_1^{SA} = 10\%$ with a reasonable performance. The SANICLAY-B model was able to reach both failure criteria but with a much steeper strength curves than the experiment. Finally, the A3-SKH model was not able to reach any of the failure criteria.

4.2.2 Variation of the initial stress ratio

The influence of the initial stress ratio in the cyclic behavior is now analyzed. For that purpose, undrained cyclic triaxial tests C26-C29 on normally consolidated samples with constant deviatoric stress amplitude of $q^{amp} = 30$ kPa and anisotropic initial stress ratios $\eta_0 = \{0.25, 0.125, -0.125, -0.25\}$ are considered. The experiments followed an initial isotropic consolidation until $p_0 = 200$ kPa. Then, the axial stress was increased or decreased to achieve the desired initial stress ratio η_0, where the anisotropic consolidation was performed. The experimental results are presented in Figs. 10a–d and 11a–d, and suggest that greater magnitude of the initial stress ratio $|\eta_0|$ generates a faster accumulation of vertical strains, and therefore, a reduction in the number of cycles to reach failure conditions.

Simulations results with the CAM model showed an accurate accumulation of vertical strains and pore water pressure. Some small discrepancies are found in the reduction of the mean effective pressure upon cycles in test C29, with the lower initial stress ratio, see Fig. 10h. The mentioned discrepancy suggests once more, that the rotation rate of the historiotropic surface in extension should differ from that in compression. On the other hand, simulations results with the AHP+ISA model show an overestimation of vertical strains and pore water pressure accumulation during the first cycles in tests with initial average stress ratios in the triaxial compression regime ($\eta_0 > 0$). In addition, an underestimation of vertical strains and pore water pressure accumulation was found on test C29. This opens the discussion whether parameter β, controlling the strain amplitude required to degrade the stiffness, depends on the stress ratio. Simulations with the SANICLAY-B model suggest an excessive accumulation of vertical strains in all tests with anisotropic consolidation ($\eta_0 \neq 0$). In addition, and similar to tests with isotropic initial stresses, the model only accumulates pore water pressure during the first cycles and remains constant thereafter. Simulation results with the A3-SKH model also suggest an excessive strain accumulation in all tests of this series. Furthermore, the model reproduced lower pore water pressure accumulation on tests C26 and C29 with higher magnitudes of the initial stress ratio $|\eta_0|$, which is opposite to the observed behaviour in the experiments after 150 cycles. A summary of the excess pore water pressure curves is presented in Fig. 12, and suggests that the performance of the models is less accurate on tests with anisotropic consolidation than in tests with isotropic consolidation.

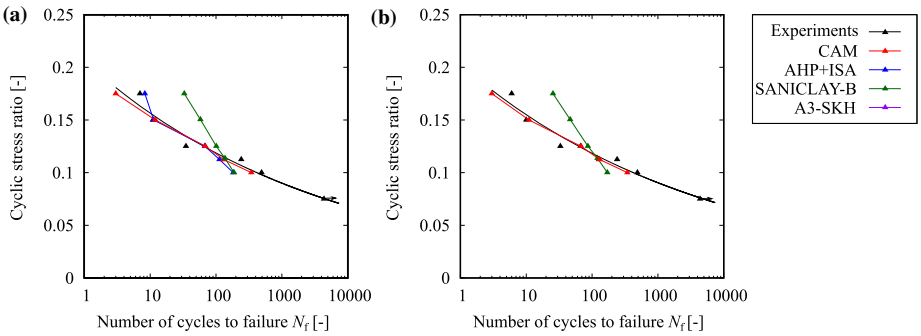

Fig. 9 CSR-N_f curves for different failure criteria: **a** $\varepsilon_1^{SA} = 10\%$, **b** $\varepsilon_1^{DA} = 10\%$

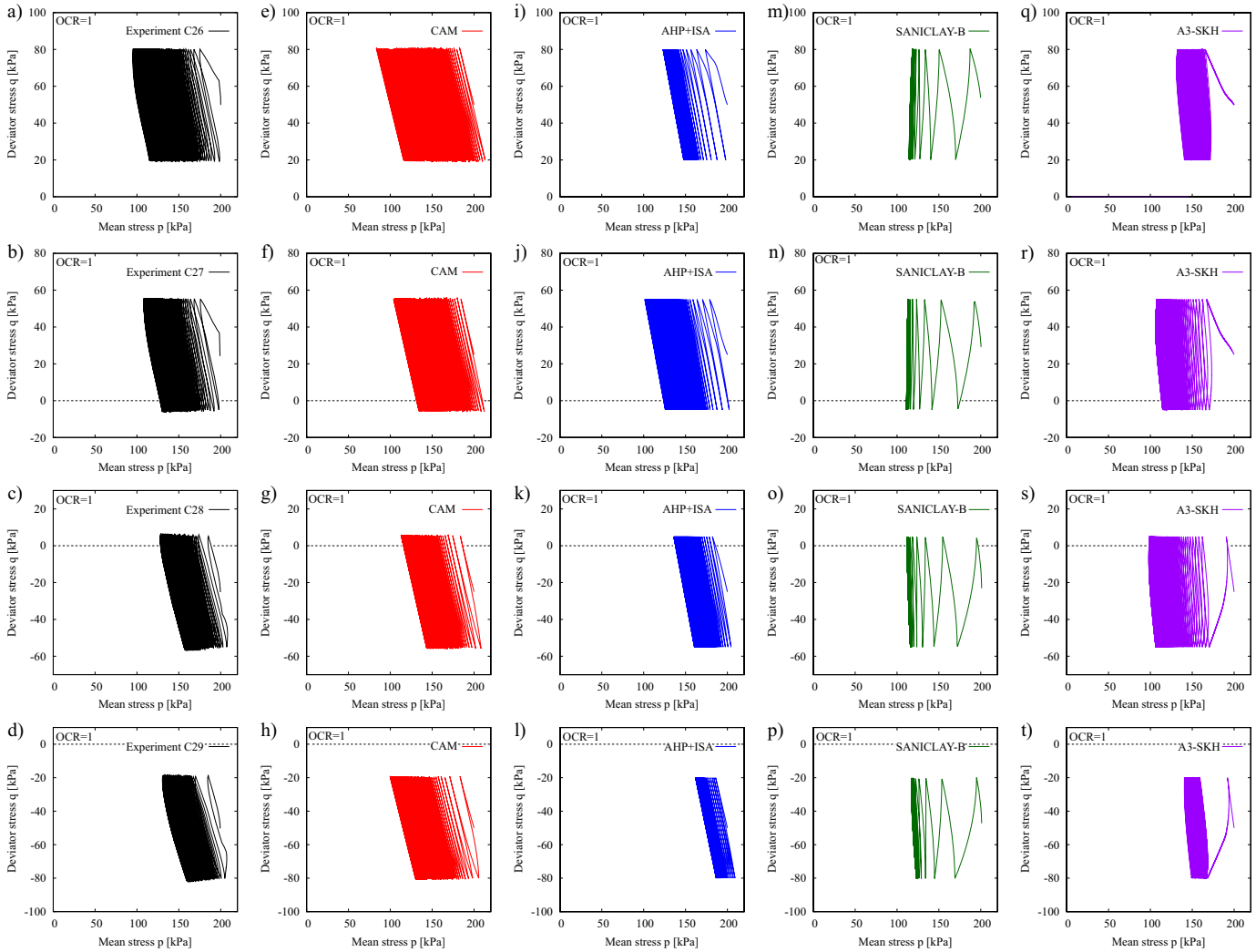

Fig. 10 Simulations of undrained cyclic triaxial tests C26-C29 on normally consolidated samples with constant deviatoric stress amplitude $q^{\text{amp}} = 30$ kPa, variation of the initial stress ratio $\eta_0 = \{0.25, 0.125, -0.125, -0.25\}$ and $p_0 = 200$ kPa, $q - p$ space: **a–d** experiments by Wichtmann and Triantafyllidis [68], **e**, **h** CAM, **i–l** AHP+ISA, **m–p** SANICLAY-B, **q–t** A3-SKH

4.2.3 Variation of the initial overconsolidation ratio

The influence of the initial overconsolidation ratio on the behavior under cyclic loading is of crucial interest, considering that most natural clay deposits are composed of strata with different OCR degrees. For that reason, experiments C37-C39 were numerically simulated considering the same initial mean effective pressure $p_0 = 100$ kPa and deviatoric stress amplitude of $q^{\text{amp}} = 30$ kPa, but preloading the samples up to reach different initial overconsolidation ratios OCR $= \{1.5, 2.0, 2.5\}$. The analysis of these tests were performed considering 115 cycles, since this was the number of cycles required in test C37 to reach failure ($\varepsilon_1^{\text{SA}} = 10\%$). Therefore, considering the same number of cycles, the influence of the initial overconsolidation ratio in the strains and pore water pressure accumulation can be easily compared in tests C38-C39.

The experimental results are presented in Figs. 13a–c and 14a–c. From these tests, it is noted, that as the initial oversonsolidation ratio increases, a higher dilatant response including negative pore pressure is in the first cycle obtained, and a reduction of the pore pressure on the subsequent cycles is observed. From the simulation results with the CAM model one may conclude, that the negative pore pressure in the first cycle was not reproduced. Despite of this, the model was able to capture fairly well the pore pressure accumulation in the subsequent cycles, resulting in a significantly less pronounced reduction of the mean effective stress with increasing initial overconsolidation ratio, as observed in the experiments. The mobilized cycles

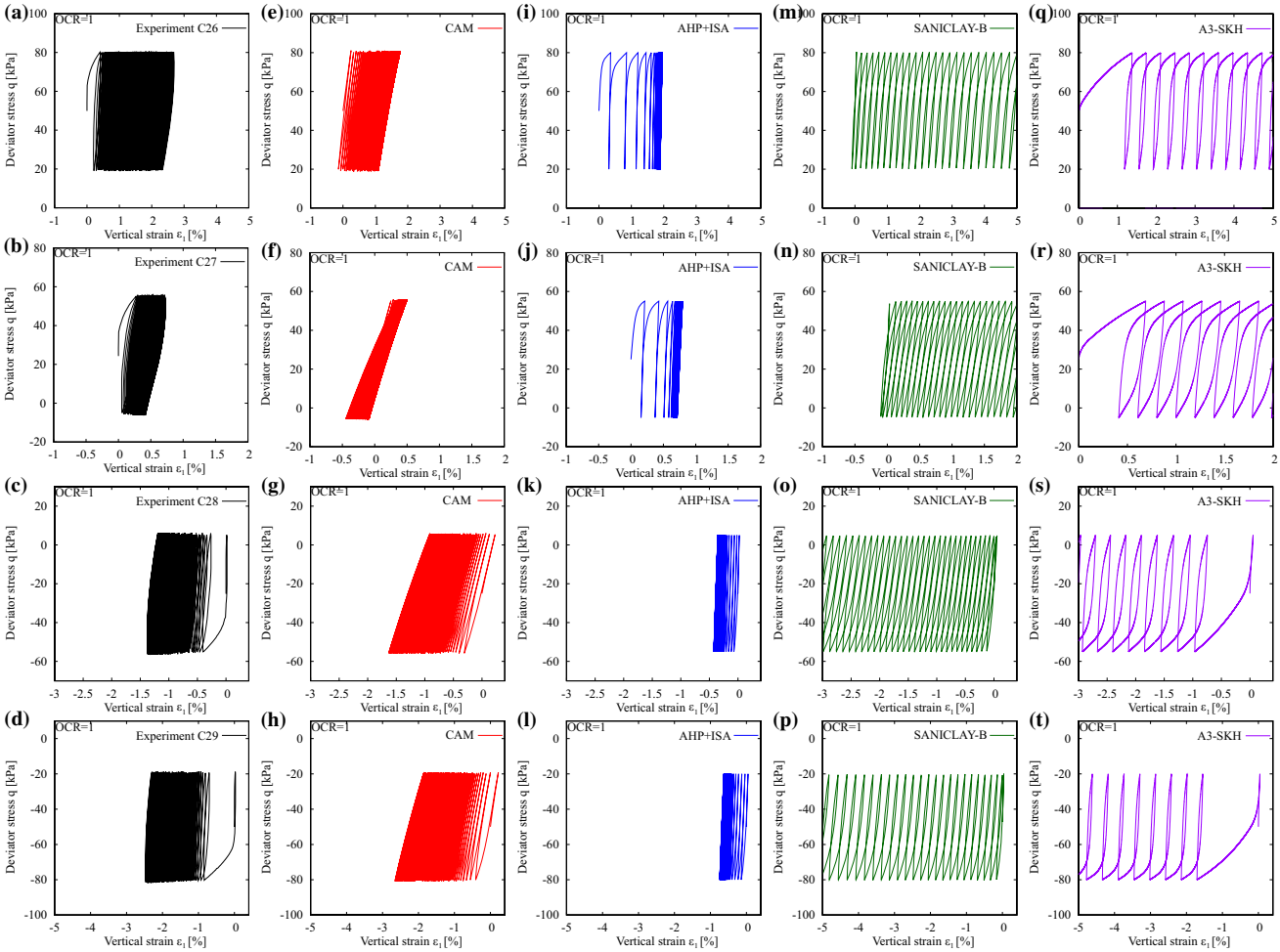

Fig. 11 Simulations of undrained cyclic triaxial tests C26-C29 on normally consolidated samples with constant deviatoric stress amplitude $q^{\text{amp}} = 30$ kPa, variation of the initial stress ratio $\eta_0 = \{0.25, 0.125, -0.125, -0.25\}$ and $p_0 = 200$ kPa, $q - \varepsilon_1$ space: **a–d** experiments by Wichtmann and Triantafyllidis [68], **e–h** CAM, **i–l** AHP+ISA, **m–p** SANICLAY-B, q-t) A3-SKH

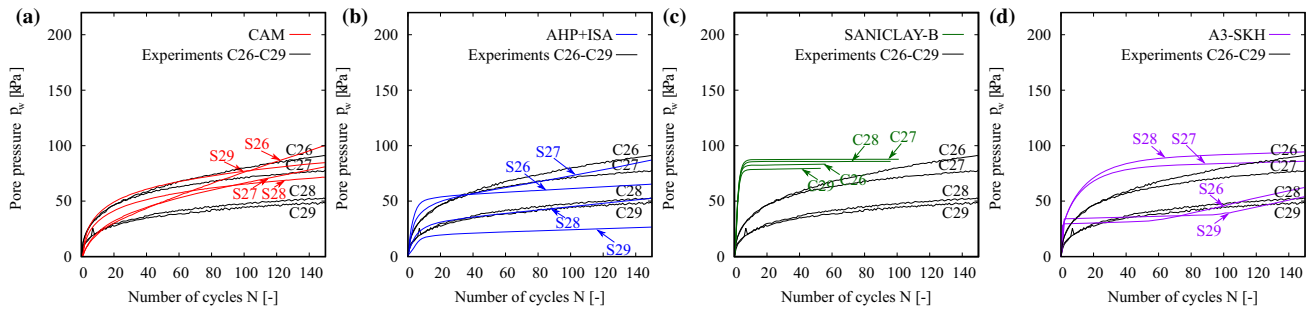

Fig. 12 Accumulated pore water pressure in the simulations of undrained cyclic triaxial tests C26-C29 on normally consolidated samples with constant deviatoric stress amplitude $q^{\text{amp}} = 30$ kPa, variation of the initial stress ratio $\eta_0 = \{0.25, 0.125, -0.125, -0.25\}$ and $p_0 = 200$ kPa: **a** CAM, **b** AHP+ISA, **c** SANICLAY-B, **d** A3-SKH

presenting eight-shaped loops in the $q - p$ space shown on test C37 was also reproduced by the CAM model. On the other hand, the AHP+ISA model managed to reach failure conditions on test C37, however, a bias in strain accumulation on the compression side was reproduced by the model and the eight-shaped loop in the $q - p$ space was not captured. Both drawbacks are explained by the non-consideration of the fabric rearrangement in the flow rule and the drastic reduction of the plastic strain rate produced by the intergranular strain formulation. Simulation results of

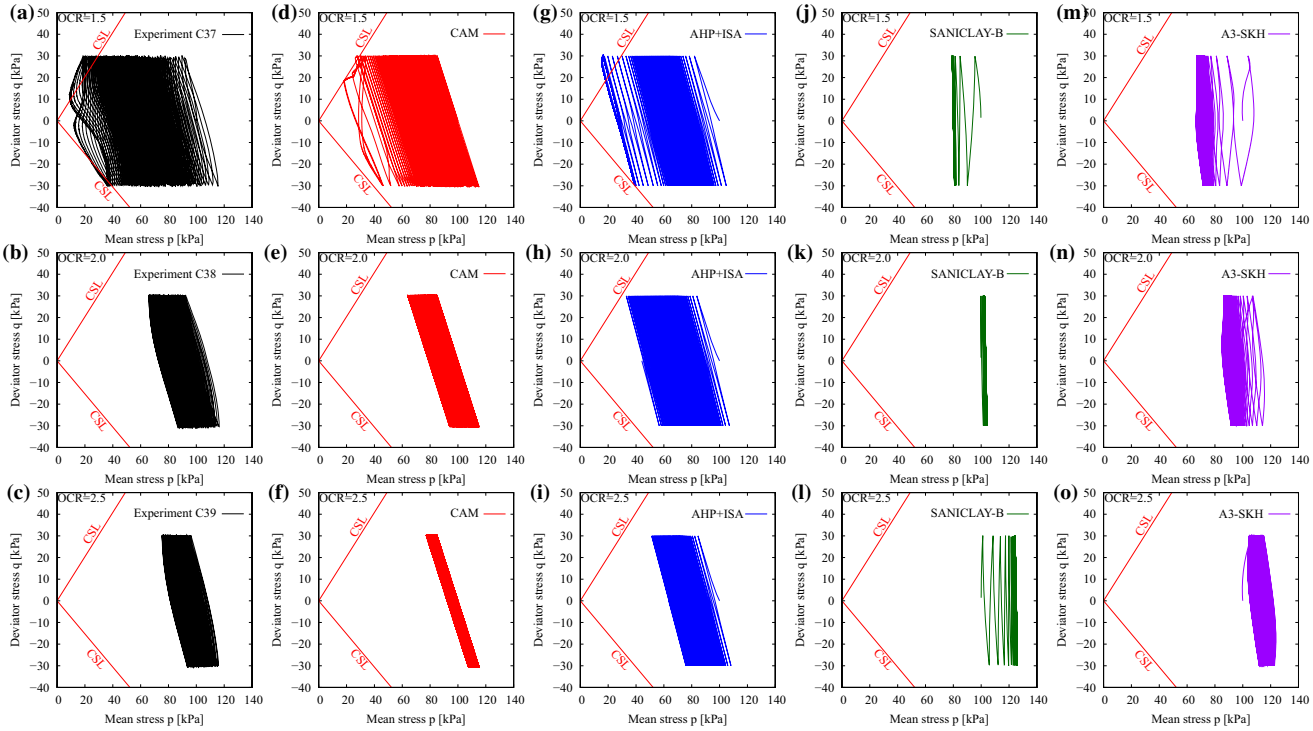

Fig. 13 Simulations of undrained cyclic triaxial tests C37-C39 with constant deviatoric stress amplitude $q^{amp} = 30$ kPa, isotropic consolidation ($p_0 = 100$ kPa, $q_0 = 0$, $\eta_0 = 0$) and variation of the initial overconsolidation ratios OCR $= \{1.5, 2.0, 2.5\}$, $q - p$ space: **a–c** experiments by Wichtmann and Triantafyllidis [68], **d–f** CAM, **g–i** AHP+ISA, **j–l** SANICLAY-B, **m–o** A3-SKH

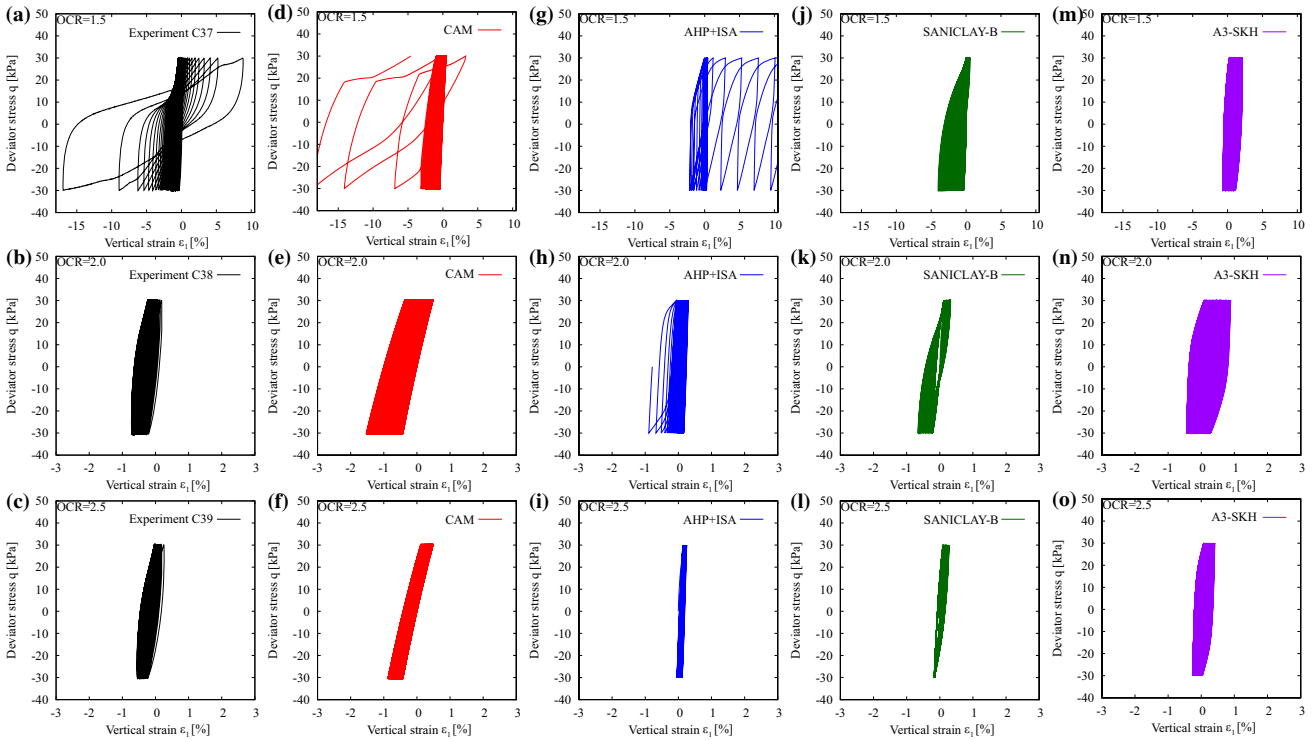

Fig. 14 Simulations of undrained cyclic triaxial tests C37-C39 with constant deviatoric stress amplitude $q^{amp} = 30$ kPa, isotropic consolidation ($p_0 = 100$ kPa, $q_0 = 0$, $\eta_0 = 0$) and variation of the initial overconsolidation ratios OCR $= \{1.5, 2.0, 2.5\}$, $q - \varepsilon_1$ space: **a–c** experiments by Wichtmann and Triantafyllidis [68], **d–f** CAM, **g–i** AHP+ISA, **j–l** SANICLAY-B, **m–o** A3-SKH

tests C38 and C39 showed a moderate reduction in the accumulation rate and an inability to reproduce the negative pore water pressure accumulation experimentally observed in the first cycle. Finally, simulation results with both SANICLAY-B as well as the A3-SKH model showed that they were able to reproduce the dilative response observed in the first cycle due to their flow rule formulation. However, simulation results of test C39, with the higher OCR, shows an always increasing negative pore water pressure, which is not observed in the experiment, see Fig. 13l,o. A summary of the pore water pressure accumulation on tests C37-C39 is presented in Fig. 15. The results suggest that the influence of the OCR on the pore water pressure accumulation is partly well predicted by the CAM model and AHP+ISA, and less accurate by the SANICLAY-B and A3-SKH models.

4.2.4 Variation of the axial strain amplitude

The next analysis corresponds to undrained cyclic triaxial tests C43-C44. In contrast to previous laboratory data, these tests were performed with strain-controlled cycles, see Figs. 16a,b and 17a,b. The kaolin samples were initially isotropically consolidated with a mean effective stress of $p_0 = 300$ kPa. Subsequently, they were cyclic loaded under a constant axial strain amplitude of $\varepsilon_1^{\text{amp}} = \{1, 2\}$ %. Note that the state with zero effective stress ($p = q = 0$) was not reached in any test. The material exhibits "fir tree" loops when approaching to failure conditions, see Fig. 16a,b. The experiments show that the increasing number of cycles leads to an increase in the excess pore water pressure accumulation and a progressive reduction of the deviatoric stress amplitude q^{amp} from its maximum magnitude in the first cycle. In addition, an increase in the cyclic axial strain amplitude of the tests generates a higher final accumulation of pore water pressure.

Simulation results with the CAM model suggest that it succeeds to reduce the mean effective stress towards an asymptotic value $p > 0$. However, after a certain number of cycles (after $N \approx 20$), the model produces higher pore pressure accumulation for lower axial strain amplitudes, which is in disagreement with the experiments. The progressive reduction of the deviatoric stress amplitude upon the cycles observed in the stress-strain space was captured by the model, although it shows a faster degradation on the extension side ($q < 0$). Simulations with the AHP+ISA model suggest similar conclusions, in which the test with the higher strain amplitude produce lower pore water pressure accumulation. However, the almost symmetric reduction of the deviatoric stress observed in the stress-strain space was much better reproduced by this model. Finally, simulation results with SANICLAY-B and A3-SKH model suggest the same findings obtained on tests with stress-controlled cycles, where the accumulation of pore water pressure is strongly reduced at $p \approx p_c/2$. Due to this attractor, the deviatoric stress amplitude was not sufficiently degraded. However, the experimental observation that the maximum deviatoric stress was reached in the first cycle, independently of the axial strain amplitude of the test, was only reproduced by the SANICLAY-B model. Fig. 18 summarizes the accumulation of the pore water pressure on tests C43-C44. In general, the influence of the cyclic axial strain amplitude is moderately reproduced by the CAM and AHP+ISA model, and much less accurate by the SANICLAY-B and A3-SKH models.

4.2.5 Variation of the cutting direction

The last simulation corresponds to the experiment C41 corresponding to an undrained cyclic triaxial test with the same initial conditions as test C4 ($p_0 = 200$ kPa, $\eta_0 = 0$, $q^{\text{amp}} = 45$ kPa) but having horizontal cutting direction of the sample (vertical bedding plane), see Fig. 2. The experimental results on test C41 are presented in Fig. 20a,b and showed a very different behavior in comparison to test C4: (a) a stiffer response, (b) the number of cycles required to reach failure conditions is considerably higher, (c) the

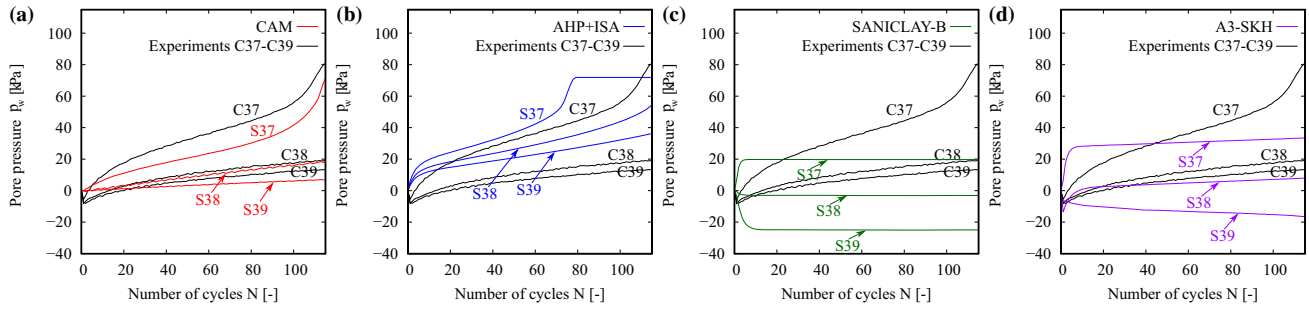

Fig. 15 Accumulated pore water pressure in the simulations of undrained cyclic triaxial tests C37-C39 with constant deviatoric stress amplitude $q^{\text{amp}} = 30$ kPa, isotropic consolidation ($p_0 = 100$ kPa, $q_0 = 0$, $\eta_0 = 0$) and variation of the initial overconsolidation ratios OCR $= \{1.5, 2.0, 2.5\}$: **a** CAM, **b** AHP+ISA, **c** SANICLAY-B, **d** A3-SKH

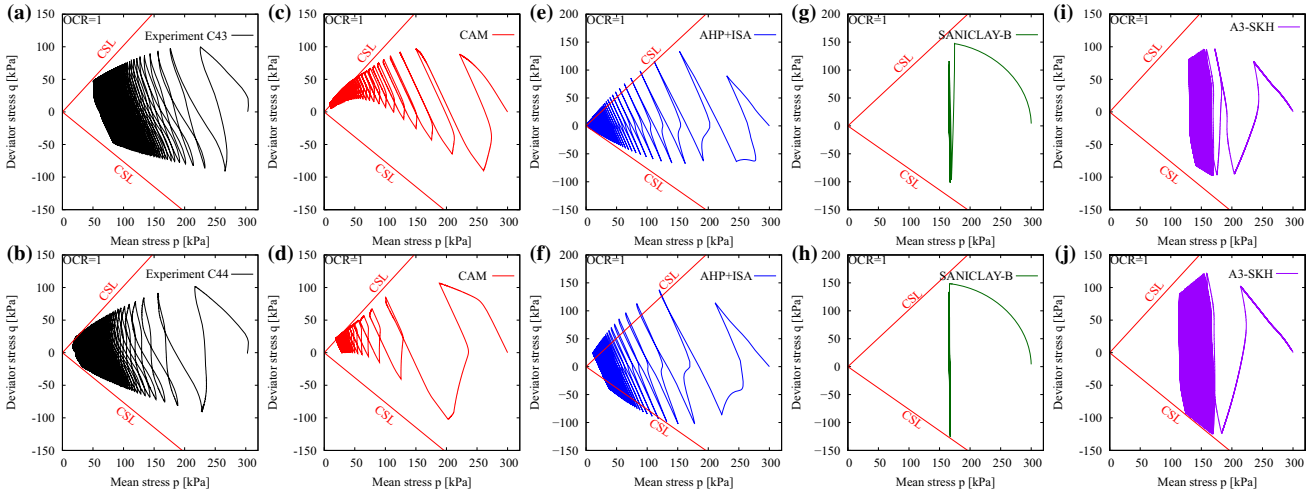

Fig. 16 Simulations of undrained cyclic triaxial tests C43-C44 on normally consolidated samples with isotropic consolidation ($p_0 = 300$ kPa, $q_0 = 0$, $\eta_0 = 0$) and variation of the axial strain cycles amplitude $\varepsilon_1^{amp} = \{1, 2\}$ %, $q - p$ space: **a**, **b** experiments by Wichtmann and Triantafyllidis [68], **c**, **d** CAM, **e**, **f** AHP+ISA, **g**, **h** SANICLAY-B, **i**, **j** A3-SKH

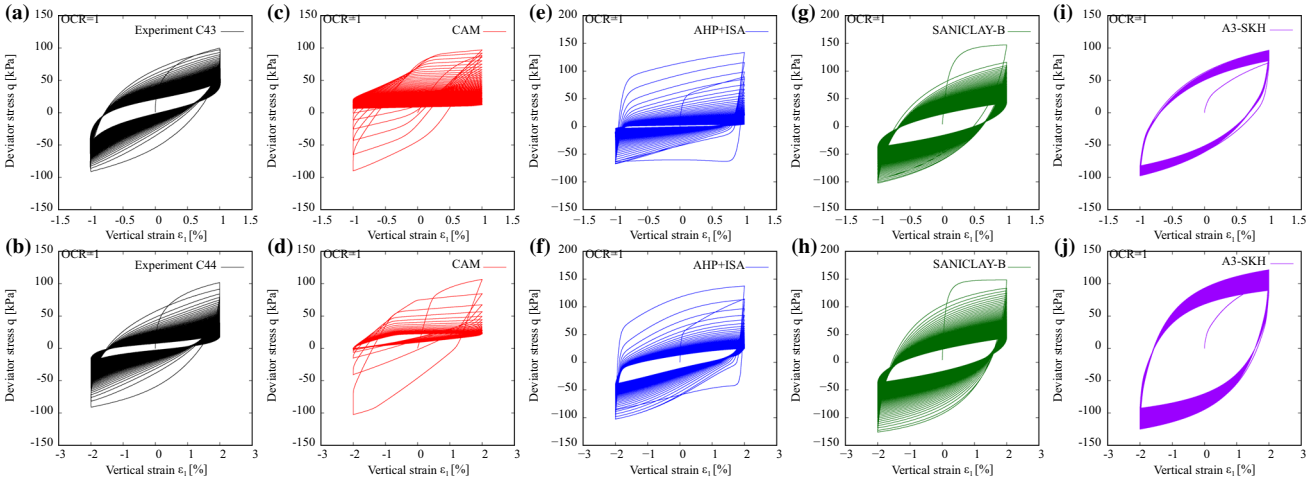

Fig. 17 Simulations of undrained cyclic triaxial tests C43-C44 on normally consolidated samples with isotropic consolidation ($p_0 = 300$ kPa, $q_0 = 0$, $\eta_0 = 0$) and variation of the axial strain cycles amplitude $\varepsilon_1^{amp} = \{1, 2\}$ %, $q - \varepsilon_1$ space: **a**, **b** experiments by Wichtmann and Triantafyllidis [68], **c**, **d** CAM, **e**, **f** AHP+ISA, **g**, **h** SANICLAY-B, **i**, **j** A3-SKH

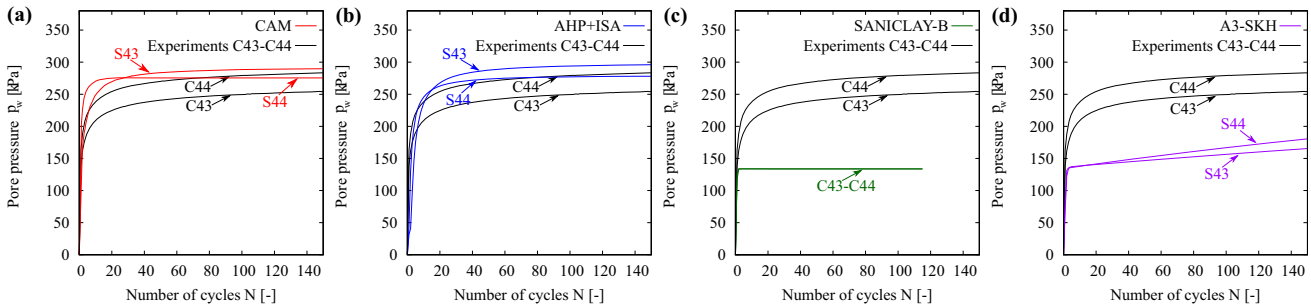

Fig. 18 Accumulated pore water pressure in the simulations of undrained cyclic triaxial tests C43-C44 on normally consolidated samples with isotropic consolidation ($p_0 = 300$ kPa, $q_0 = 0$, $\eta_0 = 0$) and variation of the axial strain cycles amplitude $\varepsilon_1^{amp} = \{1, 2\}$ %: **a** CAM, **b** AHP+ISA, **c** SANICLAY-B, **d** A3-SKH

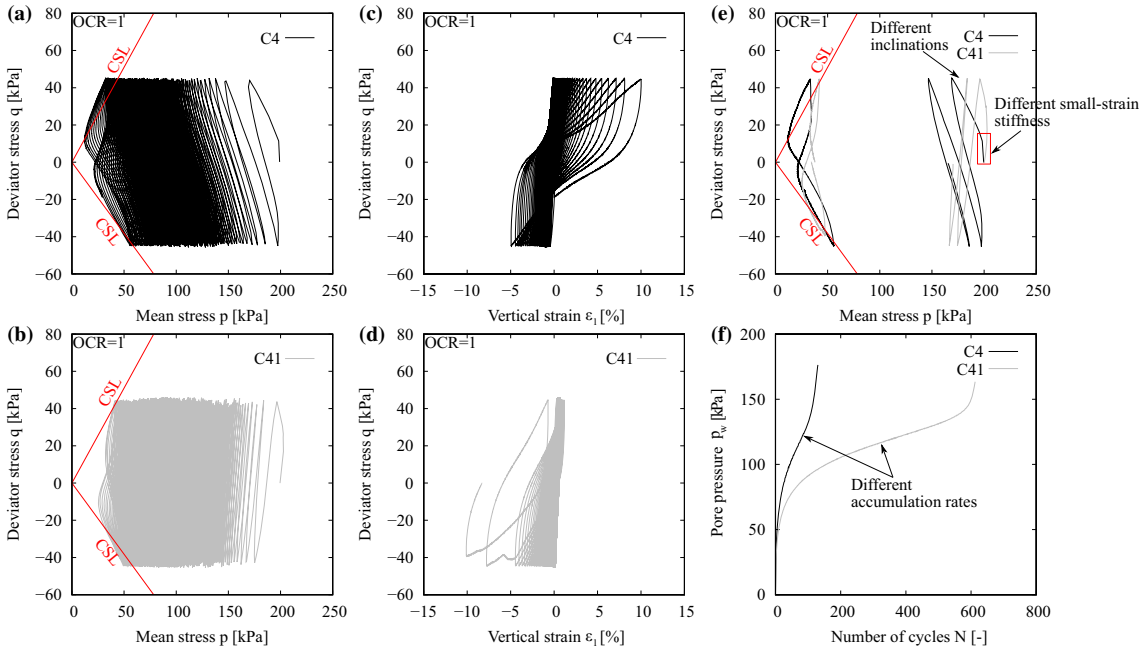

Fig. 19 Comparison of undrained cyclic triaxial tests C4 and C41 on normally consolidated samples with constant deviatoric stress amplitude $q^{amp} = 45$ kPa, isotropic consolidation ($p_0 = 200$ kPa, $q_0 = 0$, $\eta_0 = 0$) and vertical (C4) or horizontal cutting direction (C41)

strain accumulation is obtained in the extension side, and (d) the effective stress paths of the undrained cycles have an opposite inclination, see Fig. 19. All these experimental evidences are expected to be reproduced by anisotropic models for fine-grained soils. The CAM model was able to reproduce the opposite inclination of the effective stress path in the $q - p$ space. In addition, the accumulation of vertical strains as well as the excess pore water pressure accumulation were reasonably well predicted, see Figs. 20d and 21a. Also, the AHP+ISA model reproduced the inclination of the effective stress path in the $q - p$ space. In addition, the reduction of the mean effective stress was particularly well reproduced. However, an overestimation of the vertical strains was found during the first cycles, similar to the results obtained on tests with anisotropic consolidation. The SANICLAY-B model did not capture the opposite inclination as other models, considering that it does not incorporate any anisotropic elastic tensor. It also showed a much faster accumulation of pore pressures than the experiments during the first cycles.

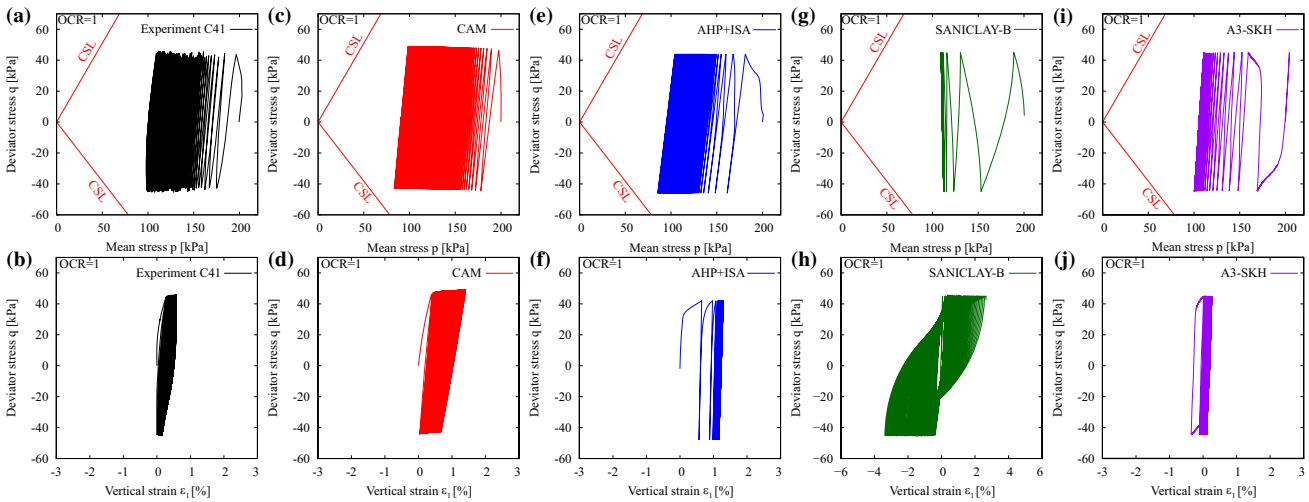

Fig. 20 Simulations of undrained cyclic triaxial test C41 on a normally consolidated sample with constant deviatoric stress amplitude $q^{amp} = 45$ kPa, isotropic consolidation ($p_0 = 200$ kPa, $q_0 = 0$, $\eta_0 = 0$) and horizontal cutting direction: **a**, **b** experiments by Wichtmann and Triantafyllidis [68], **c**, **d** CAM, **e**, **f** AHP+ISA, **g**, **h** SANICLAY-B, **i**, **j** A3-SKH

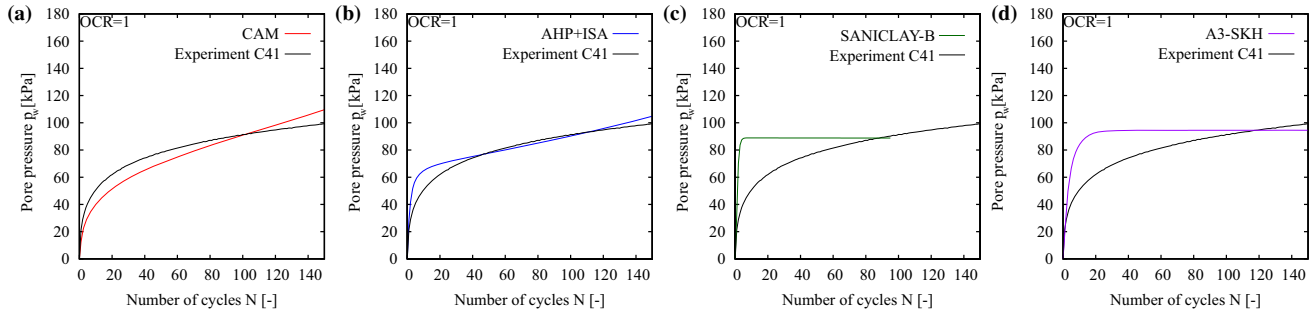

Fig. 21 Accumulated pore water pressure in the simulation of the undrained cyclic triaxial test C41 with constant deviatoric stress amplitude $q^{amp} = 45$ kPa, isotropic consolidation ($p_0 = 200$ kPa, $q_0 = 0$, $\eta_0 = 0$) and horizontal cutting direction: **a** CAM, **b** AHP+ISA, **c** SANICLAY-B, **d** A3-SKH

Finally, simulation results with the A3-SKH model captured partly well the inclination of the $p - q$ path with a less pronounced slope than the experiments. Similar to the SANICLAY-B model, the pore pressure generation on the first cycles was faster than the experiments. A summary of the accumulated pore water pressure curves are presented in Fig. 21 and suggest accurate predictions with the CAM and AHP+ISA models, while a faster accumulation with the A3-SKH and SANICLAY-B models. The experimental result in the stress-strain space is presented in Fig. 20b. It suggests that after each cycle the maximum vertical strain in compression and extension always increase, similar to tests with isotropic consolidation and vertical cutting direction, see section 4.2.1. Only the SANICLAY-B model agrees with this experimental observation but with a higher magnitude of the vertical strains. CAM and AHP+ISA models predict a lower magnitude of the vertical strain accumulation but increasing only towards compression, similar to tests with anisotropic consolidation. The vertical strain accumulation with the A3-SKH model increases during the first cycles but remains almost constant thereafter.

5 Summary and conclusions

Reliable predictions of complex geotechnical problems subjected to cyclic loading require robust constitutive models for soils, able to predict the main characteristics of the material under different conditions but employing the same set of material parameters. For that purpose, the main advantage and limitations of each constitutive model should be very well known before their application on boundary value problems. In this article, the predictions capabilities of four advanced constitutive models for anisotropic fine-grained soils, namely: CAM, AHP+ISA, SANICLAY-B and A3-SKH, were inspected under a wide range of test conditions. It is important to point out that while models AHP+ISA and CAM have been developed using the same or similar data as used for evaluation in this paper, SANICLAY-B and A3-SKH have been developed using different data. The comparison between experimental and element test results suggests the following main findings:

- The inspected models perform well under undrained monotonic loading. They were able to accurately reproduce the experimental effective stress paths and the maximum deviatoric stresses on tests with different initial mean effective pressures.
- The eight-shaped effective stress paths observed on undrained cyclic triaxial tests, with constant deviatoric stress amplitude, and with isotropic consolidation are only reproduced to some extent by the CAM model. In addition, only the SANICLAY-B model was able to realistically reproduce the always increasing double strain amplitude after cyclic mobility. While the AHP+ISA model presents a bias in the strain accumulation, the CAM model reproduced the double strain amplitude with accumulation in extension instead of compression as observed in the laboratory data. The A3-SKH model failed to reproduce the double strain amplitude. Models having problems to reproduce the behaviour at large deformations are limited in applications dealing with earthquake loading.
- The analysis of the CSR-N_f curves on cyclic undrained tests with isotropic consolidation is still a challenge with the inspected models. For their correct reproduction, two important features need to be correctly accounted: a) accurate reproduction of the influence of the deviatoric stress amplitude in the accumulation rates, and b) the capability to (at least qualitatively) reach the defined failure criteria. The first item was fairly well reproduced by the CAM and AHP+ISA models. The second item was correctly reproduced by the CAM and SANICLAY-B models. It should be remarked that the accurate performance on the first item with the CAM and AHP+ISA models is compensated

with a higher number of model parameters in comparison to the SANICLAY-B and A3-SKH models.

- Simulations on tests with different initial stress ratios suggest a less accurate performance in comparison to simulations on tests with isotropic consolidation. While the A3-SKH and SANICLAY-B models show an excessive accumulation of vertical strains, the AHP+ISA model presents an underestimation of the strains, especially on tests with initial average stress ratios in the triaxial extension regime.
- Simulation results with the inspected models suggest that the influence of the OCR on the pore water pressure accumulation is partly well predicted by the CAM model and AHP-ISA model, and moderately predicted by the SANICLAY-B and A3-SKH models.
- The degree of anisotropy plays a major role in the mechanical behavior of kaolin under cyclic loading. The experiments suggest different stiffnesses, accumulations rates and inclination of the effective stress paths depending on the cutting direction. These experimental evidences were fairly well reproduced by the CAM and AHP+ISA models, partially reproduced by the A3-SKH model and not well reproduced by the SANICLAY-B model. A simple way to fix this shortcoming of SANICLAY-B model is by scaling the isotropic hypoelastic stiffness and introducing an additional material parameter α, controlling the degree of anisotropy.
- In general, taking into account the complexity of the models, all show good agreement with the experiments. Of course, at the expense of other laboratory tests, one could reproduce each experiment more accurately using a different set of parameters. The parameter set shown in this work has been selected as the mean best fit for all experiments. This approach should also be followed for the application of the models on boundary value problems. Of course, if the loading conditions of the boundary value problem are known, then the models should be calibrated specifically based on these conditions.

Appendix

Mathematical formulation of the inspected models

CAM model

The Constitutive Anamnesis Model (CAM) by Tafili [56] presents the following general form:

$$\dot{\boldsymbol{\sigma}} = \mathsf{E} : \left(\dot{\boldsymbol{\varepsilon}} - \dot{\boldsymbol{\varepsilon}}^{\mathrm{hp}} - \dot{\boldsymbol{\varepsilon}}^{\mathrm{vis}}\right) \tag{1}$$

where the hypoplastic strain rate $\dot{\boldsymbol{\varepsilon}}^{\mathrm{hp}}$ viscous strain rate and $\dot{\boldsymbol{\varepsilon}}^{\mathrm{vis}}$ read:

$$\dot{\boldsymbol{\varepsilon}}^{\mathrm{hp}} = Y\mathbf{m} \parallel \dot{\boldsymbol{\varepsilon}} \parallel \tag{2}$$

$$\dot{\boldsymbol{\varepsilon}}^{\mathrm{vis}} = I_v \lambda \left(\frac{1}{\mathrm{OCR}}\right)^{1/I_v} \mathbf{m}, \quad \text{with} \quad \mathrm{OCR} = \frac{p_{ei}}{p^+} \tag{3}$$

with the degree of nonlinearity Y, the hypoplastic flow rule $\mathbf{m}$, the overconsolidation ratio OCR, the Hvorslev mean stress p_{ei}, the stress projection p^+, and parameters I_v and λ.

The model incorporates the following evolving historiotropic flow surface:

$$F(\boldsymbol{\sigma}, \boldsymbol{\sigma}_B) = \mathbf{w} : \mathbf{w} - \frac{2}{3} M_{\mathbf{w}}^2 \left[1 - \left(\frac{p}{p_B}\right)^{c_B}\right] \left[1 - \sqrt{\frac{3}{2}} \frac{\sqrt{\boldsymbol{\Omega} : \boldsymbol{\Omega}}}{M_{\boldsymbol{\Omega}}}\right]^2 \tag{4}$$

with the back stress tensor $\boldsymbol{\sigma}_B = p_B(-\mathbf{1} + \boldsymbol{\Omega})$, the deviatoric tensor $\mathbf{w}$, the scalar factors $M_{\mathbf{w}}$ and $M_{\boldsymbol{\Omega}}$ and parameter c_B. For a detailed definition of the variables and the equations governing the model the readers are referred to [56, 58].

The transversely isotropic tangential stiffness tensor E_{abcd} is defined as follows:

$$\mathsf{E}_{abcd} = \mathsf{Q}_{abij} : \mathsf{E}_{ijkl} : \mathsf{Q}_{klcd} \tag{5}$$

$$\mathsf{Q}_{abcd} = \mu_{ac}\mu_{bd}, \quad \text{with} \quad \mu = \sqrt{\alpha}\mathbf{1} + \left(1 - \sqrt{\alpha}\right)\mathbf{m}_s \otimes \mathbf{m}_s \tag{6}$$

$$\mathsf{E} = 3K\left(\overrightarrow{\mathbf{1}} \otimes \overrightarrow{\mathbf{1}}\right) + 2G\left(\mathsf{I}^{\mathrm{dev}}\right) \tag{7}$$

with the Kronecker delta tensor $\mathbf{1}$, the deviatoric (fourth rank) unit tensor $\mathsf{I}^{\mathrm{dev}}$, the unit vector normal to the bedding plane $\mathbf{m}_s$, the bulk modulus K, the shear modulus G and parameter α.

The degree of nonlinearity Y reads:

$$Y = (Y_0 + (1 - Y_0)Y_D)R^{-n_0} \tag{8}$$

$$Y_D = \left(\frac{\left(\hat{\boldsymbol{\sigma}}^{\mathrm{dev}} - \Omega\right)}{\left(\hat{\boldsymbol{\sigma}}^{\mathrm{dev}} - \Omega\right)^{\rightarrow} : \left(\hat{\boldsymbol{\sigma}}_f^{\mathrm{dev}} - \Omega\right)}\right)^{n_{Y,D}} \tag{9}$$

with $\hat{\boldsymbol{\sigma}} = \boldsymbol{\sigma}/\mathrm{tr}(\boldsymbol{\sigma})$ and $\hat{\boldsymbol{\sigma}}^{\mathrm{dev}} = \hat{\boldsymbol{\sigma}} - (1/3)\mathbf{1}$, the scalar functions Y_0 and R and parameter n_0. $\hat{\boldsymbol{\sigma}}_f$ is the image of the stress at the historiotropic surface. The flow rule $\mathbf{m}$ is defined as:

$$\mathbf{m} = Y_D\mathbf{m}_D + \mathbf{m}_I \exp(-1000Y_D) \tag{10}$$

with:

$$\mathbf{m}_D = \left(-\frac{1}{3}\sqrt{\frac{2}{3}} d\mathbf{1} + \left(\hat{\boldsymbol{\sigma}}^{\text{dev}} - \Omega\right)^{\rightarrow} \right)^{\rightarrow} \tag{11}$$

where $\mathbf{m}_I$ is the flow rule adjusted to radial stress compression and d is the dilatancy rule.

The evolution law for the back stress tensor $\boldsymbol{\sigma}_B$ reads

$$\dot{\boldsymbol{\sigma}}_B = \dot{p}_B(-\mathbf{1} + \Omega) + p_B\dot{\Omega} \tag{12}$$

where

$$\dot{\boldsymbol{\Omega}} = \begin{cases} C_2\left(\hat{\boldsymbol{\sigma}}^{\text{dev}} - \boldsymbol{\Omega}\right) \,||\, \dot{\boldsymbol{\varepsilon}} \,||\, R^{-n_0}, & \text{if } \|\boldsymbol{\Omega}\| < \|\boldsymbol{\sigma}_f^{\text{dev}}\| \\ C_2\left(\hat{\boldsymbol{\sigma}}_f^{\text{dev}} - \boldsymbol{\Omega}\right) \,||\, \dot{\boldsymbol{\varepsilon}} \,||\, R^{-n_0}, & \text{if } \|\boldsymbol{\Omega}\| > \|\boldsymbol{\sigma}_f^{\text{dev}}\| \end{cases} \tag{13}$$

with parameters C_2, n_0 and the image deviator stress tensor at the limit state $\hat{\boldsymbol{\sigma}}_f^{\text{dev}}$. The evolution of p_B reads:

$$\dot{p}_B = -\frac{p_B}{\lambda}\text{tr}(\dot{\boldsymbol{\varepsilon}}) - C_2(p - p_B) \,||\, \dot{\boldsymbol{\varepsilon}}^{\text{dev}} \,||\, R^{-n_0} \tag{14}$$

with parameters λ and C_2, and the following scalar factors:

$$R = \frac{p_B}{p_B^+}, \quad \text{with} \quad p_B^+ = \frac{p}{(1-D)^{1/c_B}}, \quad \text{and} \quad D = f(F(\boldsymbol{\sigma}, \Omega)) \tag{15}$$

The maximum void ratio e_i and the critical void ratio e_c read:

$$e_i = (1 + e_{i0})\left(\frac{p_{i0}}{p}\right)^{\lambda} - 1 \tag{16}$$

$$e_c = (1 + e_{c0})\left(\frac{p_{i0}}{p}\right)^{\lambda} - 1 \tag{17}$$

with the material parameters e_{c0} and e_{i0} to be calibrated at the reference pressure $p_{i0} = 100$ kPa. The complete set of equations of the CAM model can be found in Tafili [56].

AHP+ISA model

The AHP+ISA model by Fuentes et al. [18] corresponds to the hypoplastic model by Mašín [34] extended by the Intergranular Strain Anisotropy (ISA) [21, 47]. The hypoplastic model by Mašín [34] presents the following general equation:

$$\dot{\boldsymbol{\sigma}} = \mathsf{L}^{\text{hyp}} : \dot{\boldsymbol{\varepsilon}} + \mathbf{N}^{\text{hyp}} \,||\, \dot{\boldsymbol{\varepsilon}} \,||\, \tag{18}$$

where L^{hyp} and $\mathbf{N}^{\text{hyp}}$ are the (fourth rank) linear stiffness tensor and (second rank) state-dependent tensor respectively. An anisotropic stiffness tensor L^{hyp} is adopted in the model, which follows:

$$\mathsf{L}^{\text{hyp}} = f_s\left[\frac{1}{2}a_1\mathbf{1}\circ\mathbf{1} + a_2\mathbf{1}\mathbf{1} + a_3(\mathbf{p}\mathbf{1} + \mathbf{1}\mathbf{p}) + a_4\mathbf{p}\circ\mathbf{1} + a_5\mathbf{p}\mathbf{p}\right] \tag{19}$$

where the product represented by '$\circ$' is defined as $(\mathbf{p}\circ\mathbf{1})_{ijkl} = \frac{1}{2}(p_{ik}1_{jl} + p_{il}1_{jk} + p_{jl}1_{ik} + p_{jk}1_{il})$, and tensor $\mathbf{p}$ is defined as $p_{ij} = n_i n_j$. Vector n_i is a unit and normal to the bedding plane. Vector n_i usually points into the vertical direction. Functions a_i, $i = \{1, 2, 3, 4, 5\}$ are defined as:

$$a_1 = \alpha_E\left(1 - v - 2\frac{\alpha_E}{\alpha_v^2}v^2\right) \tag{20}$$

$$a_2 = \alpha_E v\left(1 + \frac{\alpha_E}{\alpha_v^2}v\right) \tag{21}$$

$$a_3 = \alpha_E v\left(\frac{1}{\alpha_v} + \frac{v}{\alpha_v} - 1 - \frac{\alpha_E}{\alpha_v^2}v\right) \tag{22}$$

$$a_4 = \alpha_E\left(1 - v - 2\frac{\alpha_E}{\alpha_v^2}v^2\right)\frac{1 - \alpha_G}{\alpha_G} \tag{23}$$

$$a_5 = \alpha_E\left(1 - \frac{\alpha_E}{\alpha_v^2}v^2\right) + 1 - v^2 - 2\frac{\alpha_E}{\alpha_v}v(1+v) - \frac{2\alpha_E}{\alpha_G}\left(1 - v - 2\frac{\alpha_E}{\alpha_v^2}v^2\right) \tag{24}$$

where $\alpha_G = G_{pp}/G_{tp}$, $\alpha_E = E_p/E_t$ and $\alpha_v = v_{pp}/v_{tp}$ are ratios of shear moduli G_{ij}, Young moduli E_i and Poisson ratios v_{ij} respectively ($v = v_{pp}$ for simplicity), the subscript '$_p$' denotes direction within the plane of isotropy (bedding plane) and subscript '$_t$' denotes the direction transverse to the plane of isotropy. Factor f_s is defined as:

$$f_s = -\frac{3\text{tr}\boldsymbol{\sigma}}{2A_m}\left(\frac{1}{\lambda^*} + \frac{1}{\kappa^*}\right) \tag{25}$$

where A_m is defined as:

$$A_m = v^2\left(\frac{4\alpha_E}{\alpha_v} - 2\alpha_E^2 + 2\frac{\alpha_E^2}{\alpha_v^2} - 1\right) + v\left(\frac{4\alpha_E}{\alpha_v} + 2\alpha_E\right) + 2\alpha_E + 1 \tag{26}$$

Tensor $\mathbf{N}^{\text{hyp}}$ is calculated from the following set of equations:

$$\mathbf{N}^{\text{hyp}} = -\frac{f_d}{f_d^A}\left[\mathsf{L}^{\text{hyp}} + \frac{\boldsymbol{\sigma}\otimes\mathbf{1}}{\lambda^*}\right] : \frac{\boldsymbol{d}^A}{\|\boldsymbol{d}^A\|} \tag{27}$$

$$f_d = \left(\frac{2p}{p_e}\right)^{\alpha_f}, \quad p_e = p_r \exp\left[\frac{N - \ln(1+e)}{\lambda^*}\right], \quad f_d^A = 2^{\alpha_f}(1 - F_m)^{\alpha_f/\omega} \tag{28}$$

$$\omega = -\frac{\ln(\cos^2\varphi_c)}{\ln 2} + a\left(F_m - \sin^2\varphi_c\right), \quad F_m = \frac{9I_3 + I_1 I_2}{I_3 + I_1 I_2} \tag{29}$$

$$m_R = p_r A_g \left(\frac{p}{p_r}\right)^{n_g} \frac{4A_m\alpha_G}{2p\alpha_E} \left(\frac{\lambda^*\kappa^*}{\lambda^* + \kappa^*}\right)\left(1 - v - 2\frac{\alpha_E}{\alpha_v^2}v^2\right)^{-1} \tag{30}$$

$$I_1 = \mathrm{tr}\boldsymbol{\sigma}, \qquad I_2 = \frac{1}{2}\left[\boldsymbol{\sigma} : \boldsymbol{\sigma} - (I_1)^2\right], \qquad I_3 = \det\boldsymbol{\sigma} \tag{31}$$

$$\boldsymbol{d}^A = -\hat{\boldsymbol{\sigma}}^{\mathrm{dev}} + \mathbf{1}\left[\frac{2}{3} - \frac{\cos 3\theta + 1}{4}F_m^{1/4}\right] \frac{F_m^{\xi/2} - \sin^\xi\varphi_c}{1 - \sin^\xi\varphi_c} \tag{32}$$

$$\cos 3\theta = -\sqrt{6}\frac{\mathrm{tr}\left(\hat{\boldsymbol{\sigma}}^{\mathrm{dev}} \cdot \hat{\boldsymbol{\sigma}}^{\mathrm{dev}} \cdot \hat{\boldsymbol{\sigma}}^{\mathrm{dev}}\right)}{\left[\hat{\boldsymbol{\sigma}}^{\mathrm{dev}} : \hat{\boldsymbol{\sigma}}^{\mathrm{dev}}\right]^{3/2}} \tag{33}$$

$$\alpha_f = \ln\left[\frac{\lambda^* - \kappa^*}{\lambda^* + \kappa^*}\left(\frac{3 + a_f^2}{a_f\sqrt{3}}\right)\right]/\ln 2, \quad a_f = \frac{\sqrt{3}(3 - \sin\varphi_c)}{2\sqrt{2}\sin\varphi_c} \tag{34}$$

$$\hat{\boldsymbol{\sigma}} = \frac{\boldsymbol{\sigma}}{\mathrm{tr}(\boldsymbol{\sigma})}, \quad \hat{\boldsymbol{\sigma}}^{\mathrm{dev}} = \hat{\boldsymbol{\sigma}} - \frac{1}{3}\mathbf{1} \tag{35}$$

The extension ISA reformulates the model as follows:

$$\dot{\boldsymbol{\sigma}} = \mathsf{M} : \dot{\boldsymbol{\varepsilon}} \tag{36}$$

$$\mathsf{M} = \begin{cases} m(\mathsf{L}^{\mathrm{hyp}} + \rho^\chi \mathbf{N}^{\mathrm{hyp}}\mathbf{N}) & for F_H = 0 \quad \text{(plastic)} \\ m_R\mathsf{L}^{\mathrm{hyp}} & for F_H < 0 \quad \text{(elastic)} \end{cases} \tag{37}$$

The rate of the intergranular strain $\mathbf{h}$ follows:

$$\dot{\mathbf{h}} = \dot{\boldsymbol{\varepsilon}} - \dot{\lambda}_H\mathbf{N}, \quad \text{with} \quad \mathbf{N} = (\mathbf{h} - \mathbf{c})^{\rightarrow}, \quad \text{and} \quad \dot{\lambda}_H = \frac{\langle \mathbf{N} : \dot{\boldsymbol{\varepsilon}}\rangle}{1 + \mathbf{N} : \bar{\mathbf{c}}} \tag{38}$$

The yield and bounding surfaces are defined as

$$F_H = \| \mathbf{h} - \mathbf{c} \| - R/2 \qquad \text{(yield surface)} \tag{39}$$

$$F_b = \| \mathbf{h} \| - R \qquad \text{(bounding surface)} \tag{40}$$

The center of the yield surface $\mathbf{c}$ evolves according to the following hardening equation:

$$\dot{\mathbf{c}} = \dot{\lambda}_H\bar{\mathbf{c}}, \quad \bar{\mathbf{c}} = \beta_h(\mathbf{c}_b - \mathbf{c})/R, \quad \mathbf{c}_b = (R/2)\overrightarrow{\dot{\boldsymbol{\varepsilon}}} \tag{41}$$

The following scalar factors are used:

$$m = m_R + (1 - m_R)y_h, \qquad y_h = \rho^\chi\langle \mathbf{N} : \dot{\boldsymbol{\varepsilon}}\rangle, \quad \rho = 1 - \frac{\|R\mathbf{N} - \mathbf{h}\|}{2R} \tag{42}$$

Finally, the following modification by [47] is also used:

$$\chi = \chi_0 + \varepsilon_{\mathrm{acc}}(\chi_{\max} - \chi_0), \quad \dot{\varepsilon}_{\mathrm{acc}} = \frac{c_a}{R}\left((1 - y_h)^2 - \varepsilon_{\mathrm{acc}}\right) \| \dot{\boldsymbol{\varepsilon}} \| \tag{43}$$

$$\beta_h = \beta_{\mathrm{hmax}} + (\beta_{h0} - \beta_{\mathrm{hmax}}) \mid \overrightarrow{\mathbf{h}_b} : \overrightarrow{\mathbf{d}_b} \mid \tag{44}$$

SANICLAY-B model

The SANICLAY-B model presents the following general elastoplastic form:

$$\dot{\boldsymbol{\sigma}} = \boldsymbol{\mathcal{D}}^e : (\dot{\boldsymbol{\varepsilon}} - \dot{\boldsymbol{\varepsilon}}^p) \tag{45}$$

where the elastic stiffness tensor $\boldsymbol{\mathcal{D}}^e$ is formulated provide the following isotropic elastic relations:

$$\dot{\varepsilon}_v^e = \frac{\dot{p}}{K} \qquad \dot{\varepsilon}_s^e = \frac{\dot{q}}{3G} \tag{46}$$

where $\dot{\varepsilon}_v^e$ and $\dot{\varepsilon}_s^e$ are the volumetric and deviatoric elastic strain invariants, respectively, $K = p(1 + e_{\mathrm{ini}})/\kappa$ is the elastic Bulk modulus, κ is a parameter, e_{ini} is the initial void ratio, and the elastic shear modulus G can be expressed in terms of K and the poisson ratio v.

The bounding surface F and the plastic potential surface G are defined as:

$$F = \frac{3}{2}(\bar{\mathbf{s}} - \bar{p}\boldsymbol{\alpha}) : (\bar{\mathbf{s}} - \bar{p}\boldsymbol{\alpha}) - \left(N^2 - \frac{3}{2}\boldsymbol{\alpha} : \boldsymbol{\alpha}\right)\bar{p}(p_0 - \bar{p}) = 0 \tag{47}$$

$$G = \frac{3}{2}(\bar{\mathbf{s}} - \bar{p}\boldsymbol{\alpha}) : (\bar{\mathbf{s}} - \bar{p}\boldsymbol{\alpha}) - \left(M^2 - \frac{3}{2}\boldsymbol{\alpha} : \boldsymbol{\alpha}\right)\bar{p}(p_\alpha - \bar{p}) = 0 \tag{48}$$

where N and M are parameters, $\bar{p}$ and $\bar{\mathbf{s}}$ are stress projections, and θ is the Lode angle defined as:

$$\cos(3\theta) = \sqrt{6}\mathrm{tr}\bar{\mathbf{n}}^3 \tag{49}$$

where $\bar{\mathbf{n}}$ is a unit norm deviatoric tensor along $\bar{\mathbf{r}} - \boldsymbol{\alpha}$, with $\bar{\mathbf{r}} = \bar{\mathbf{s}}/\bar{p}$. The stress projections $\bar{p}$ and $\bar{\mathbf{s}}$ are computed according to the following mapping rule:

$$\bar{p} = p_{\mathrm{c}} + b(p - p_{\mathrm{c}}), \quad \text{and} \quad \bar{\mathbf{s}} = \mathbf{s}_{\mathrm{c}} + b(\mathbf{s} - \mathbf{s}_{\mathrm{c}}) \tag{50}$$

where b is a scalar function. The loading index L in the multiaxial stress space is defined based on the consistency condition on the bounding surface as:

$$L = (\partial F/\partial \bar{\boldsymbol{\sigma}}) : \dot{\boldsymbol{\sigma}}/K_p \tag{51}$$

where K_p is the bounding plastic modulus. The evolution equations of $\dot{p}_c$ and $\dot{\mathbf{s}}_c$ read:

$$\begin{aligned}\dot{p}_c &= \frac{p_c}{p_0}\dot{p}_0, \quad \text{and}\\ \dot{\mathbf{s}}_c &= \frac{\mathbf{s}_c}{p_0}\dot{p}_0\\ &+ \left[p_c\dot{\boldsymbol{\alpha}} - X\sqrt{\frac{2}{3}}\frac{p_c(p_0-p_c)(3/2)\boldsymbol{\alpha}:\dot{\boldsymbol{\alpha}}}{\left[(N^2-(3/2)\boldsymbol{\alpha}:\boldsymbol{\alpha})p_c(p_0-p_c)\right]^{1/2}}\mathbf{n}_c\right]\end{aligned} \tag{52}$$

$$X = \left[\frac{(\mathbf{s}_c-\mathbf{s}_\alpha):(\mathbf{s}_c-\mathbf{s}_\alpha)}{(\mathbf{s}_b-\mathbf{s}_\alpha):(\mathbf{s}_b-\mathbf{s}_\alpha)}\right]^{1/2}, \quad \text{with} \quad \mathbf{s}_\alpha = p_c\boldsymbol{\alpha}, \quad \text{and} \quad \mathbf{s}_b = \mathbf{s}_\alpha + \mathbf{n}_c a_b \tag{53}$$

where

$$\mathbf{n}_c = (\mathbf{s}_c-\mathbf{s}_\alpha)/\mid \mathbf{s}_c-\mathbf{s}_\alpha \mid \tag{54}$$

$$a_b = \left[(N^2-(3/2)\boldsymbol{\alpha}:\boldsymbol{\alpha})p_c(p_0-p_c)/((3/2)\mathbf{n}_c:\mathbf{n}_c)\right]^{1/2} \tag{55}$$

The damage parameter d follows

$$\dot{d} = a_d[(2/3)\boldsymbol{e}^p:\boldsymbol{e}^p]^{1/2} \tag{56}$$

and affects directly the plastic modulus. The remaining equations, such as the yield surface, hardening rules for p_0, $\boldsymbol{\alpha}$ and the isotopic destructuration mechanism are the ones of previous SANICLAY versions by Dafalias et al. [11] and Taiebat et al. [65], respectively.

A3-SKH model

The three surface kinematic hardening (3-SKH) model proposed by Stallebras and Taylor [54, 55] follows:

$$\dot{\boldsymbol{\sigma}} = \boldsymbol{\mathcal{D}}^e : (\dot{\boldsymbol{\varepsilon}} - \dot{\boldsymbol{\varepsilon}}^p) \tag{57}$$

where $\dot{\boldsymbol{\varepsilon}}$ is the strain rate tensor and $\boldsymbol{\mathcal{D}}^e$ is the elastic tangent stiffness tensor which is defined for isotropic elastic conditions as:

$$\begin{aligned}\boldsymbol{\mathcal{D}}^e &= \left(K - \frac{2}{3}G\right)\mathbf{1}\otimes\mathbf{1} + 2G\mathbf{I}, \quad \text{with}\\ \frac{G}{p_r} &= A_g\left(\frac{p}{p_r}\right)^{n_g}(\mathrm{OCR})^m, \quad \text{and} \quad K = \frac{p}{\kappa^*}\end{aligned} \tag{58}$$

The yield function of the model is given by:

$$f(\boldsymbol{\sigma}, a, \boldsymbol{\sigma}_b) = \frac{1}{2}\left[\left(\frac{\bar{q}_b}{M}\right)^2 + \bar{p}_b^2 - T^2S^2a^2\right] \tag{59}$$

For stress states on the yield surface, the plastic strain rate is given by the following associative flow rule:

$$\begin{aligned}\dot{\boldsymbol{\varepsilon}}^p &= \frac{\langle \boldsymbol{P}:\boldsymbol{\mathcal{D}}^e:\dot{\boldsymbol{\varepsilon}}\rangle}{H + \boldsymbol{P}:\boldsymbol{\mathcal{D}}^e:\boldsymbol{P}}\boldsymbol{P}\\ \boldsymbol{P} &= \frac{\partial f}{\partial \boldsymbol{\sigma}}\end{aligned} \tag{60}$$

where H is the plastic modulus. The bounding surface is defined as:

$$F(\boldsymbol{\sigma}, a) = \frac{1}{2}\left[\left(\frac{q}{M}\right)^2 + p^2 - 2pa\right] \tag{61}$$

The second surface, called history surface, is given by:

$$f_h(\boldsymbol{\sigma}, a, \boldsymbol{\sigma}_a) = \frac{1}{2}\left[\left(\frac{\bar{q}_a}{M}\right)^2 + \bar{p}_a^2 - T^2a^2\right] \tag{62}$$

The internal scalar variable a evolves according to:

$$\dot{a} = \frac{a}{\lambda^* - \kappa^*}\dot{\boldsymbol{\varepsilon}}^p : \mathbf{1} \tag{63}$$

The kinematic hardening rules for the two back-stress tensors are given as follows:

- Plastic loading conditions with $f_h < 0$ and $F < 0$:

$$\begin{aligned}\dot{\boldsymbol{\sigma}}_a &= \frac{\dot{a}}{a}\boldsymbol{\sigma}_a,\\ \dot{\boldsymbol{\sigma}}_b &= \frac{\dot{a}}{a}\boldsymbol{\sigma}_b + \dot{Z}_s\boldsymbol{\gamma}\end{aligned} \tag{64}$$

where

$$\begin{aligned}\boldsymbol{\gamma} &= \frac{\boldsymbol{\sigma}-\boldsymbol{\sigma}_b}{S} + \boldsymbol{\sigma}_a - \boldsymbol{\sigma},\\ \dot{Z}_s &= \frac{1}{\boldsymbol{P}:\boldsymbol{\gamma}}\left[\boldsymbol{P}:\left(\dot{\boldsymbol{\sigma}} - \frac{\dot{a}}{a}\boldsymbol{\sigma}_b\right) - T^2S^2a\dot{a}\right]\end{aligned} \tag{65}$$

- Plastic loading conditions with $f_h = 0$ and $F < 0$:

$$\dot{\boldsymbol{\sigma}}_a = \frac{\dot{a}}{a}\boldsymbol{\sigma}_a + \dot{W}_s\boldsymbol{\beta} \tag{66}$$

where

$$\begin{aligned}\boldsymbol{\beta} &= \frac{\boldsymbol{\sigma}-\boldsymbol{\sigma}_b}{TS} + a\mathbf{1} - \frac{\boldsymbol{\sigma}-\boldsymbol{\sigma}_b}{S} - \boldsymbol{\sigma}_a,\\ \dot{W}_s &= \frac{1}{\boldsymbol{P}:\boldsymbol{\beta}}\left[\boldsymbol{P}:\left(\dot{\boldsymbol{\sigma}} - \frac{\dot{a}}{a}\boldsymbol{\sigma}_a\right) - T^2S^3a\dot{a}\right]\end{aligned} \tag{67}$$

The center of the yield surface, $\boldsymbol{\sigma}_b$ is now calculated explicitly from the non-intersection condition, as:

$$\boldsymbol{\sigma}_b = \boldsymbol{\sigma} - S(\boldsymbol{\sigma} - \boldsymbol{\sigma}_a) \tag{68}$$

- Plastic loading conditions with $f_h = 0$ and $F = 0$:

In this case, both back-stresses $\boldsymbol{\sigma}_a$ and $\boldsymbol{\sigma}_b$ can be

obtained in closed form from the non-intersection condition, as:

$$\begin{aligned}\boldsymbol{\sigma}_a &= \boldsymbol{\sigma} - T(\boldsymbol{\sigma} - a\mathbf{1}),\\ \boldsymbol{\sigma}_b &= \boldsymbol{\sigma} - TS(\boldsymbol{\sigma} - a\mathbf{1})\end{aligned} \tag{69}$$

The plastic modulus H is given by

$$H = h_0 + H_1 + H_2 \tag{70}$$

where

$$h_0 = -\boldsymbol{P} : \left[\frac{1}{\lambda^* - \kappa^*}\left(-T^2S^2a^2 - \boldsymbol{P} : \boldsymbol{\sigma}_b\right)\right] \tag{71}$$

$$\begin{aligned}H_1 &= S^2\left(\frac{b_1}{b_{1\max}}\right)^{\psi}\frac{a^3}{\lambda^* - \kappa^*}\\ H_2 &= \left(\frac{Tb_2}{b_{2\max}}\right)^{\psi}\frac{a^3}{\lambda^* - \kappa^*}\end{aligned} \tag{72}$$

$$\begin{aligned}b_1 &= \frac{\boldsymbol{\beta} : \boldsymbol{P}}{TSa}\\ b_2 &= \frac{\boldsymbol{\gamma} : \boldsymbol{P}}{TSa}\end{aligned} \tag{73}$$

$$\begin{aligned}b_{1\max} &= 2a(1 - T)\\ b_{2\max} &= 2Ta(1 - S)\end{aligned} \tag{74}$$

Table 6 Experimental tests, stress path sequence in terms of the invariants $p - q$ and resulting experimental oversonsolidation ratio before the undrained shearing stage

Test	Stress path sequence (p,q)	OCR [-]
M1	(5,0) → (66.5,0) → (50,0)	1.33
M2	(5,0) → (100,0)	1.00
M3	(5,0) → (200,0)	1.00
M4	(5,0) → (300,0)	1.00
M5	(5,0) → (400,0)	1.00
C1	(5,0) → (200,0)	1.00
C2	(5,0) → (200,0)	1.00
C4	(5,0) → (200,0)	1.00
C5	(5,0) → (200,0)	1.00
C7	(5,0) → (200,0)	1.00
C8	(5,0) → (200,0)	1.00
C26	(5,0) → (200,0) → (200,50)	1.00
C27	(5,0) → (200,0) → (200,25)	1.00
C28	(5,0) → (200,0) → (200,-25)	1.00
C29	(5,0) → (200,0) → (200,-50)	1.00
C37	(5,0) → (150,0) → (100,0)	1.50
C38	(5,0) → (200,0) → (100,0)	2.00
C39	(5,0) → (250,0) → (100,0)	2.50
C41	(5,0) → (200,0)	1.00
C43	(5,0) → (300,0)	1.00
C44	(5,0) → (300,0)	1.00

The A3-SKH model adopted the transverse isotropic elasticity relations proposed by Graham and Houlsby [25], using the proposed shear modulus for the plane parallel to the sedimentation axis $G_{tp} = G$.

Initialization of state variables and description of strain/stress paths

The information related to the initial stress states and initial state variables required to reproduce the simulations are provided in this section. For the sake of clarity, Table 6 includes the test code, the stress path sequence in terms of the invariants $p - q$ and the resulting experimental oversonsolidation ratio OCR before the undrained shearing stage.

Simulations reproduced the preloading consolidation reported in Table 6 before the undrained shearing. For the reproduction of the preloading consolidation path, all models were initialized with an overconsolidation ratio equal to one (OCR= 1), an initial effective stress of $p_{\text{ini}} =$ 5 kPa, and an initial deviatoric stress of $q_{\text{ini}} = 0$. The initial void ratio e_{ini} was solved from the compression relation adopted by each model by setting OCR= 1 at $p = p_{\text{ini}}$. For the particular case of the oedometric test, all models were initialized with the same initial conditions as by the experiment $e_0 = 1.424$ and $\sigma_1 = 6$ kPa, $\sigma_2 = \sigma_3 = K_0\sigma_1$ with $K_0 = 1 - \sin\varphi_c$. The state variables of each model were initialized as follows:

For the AHP+ISA model, the state variable tensors $\mathbf{h}$ and $\mathbf{c}$ were initialized as $\mathbf{h} = \mathbf{0}$ and $\mathbf{c} = \mathbf{0}$ at $p = p_{\text{ini}}$. For the oedometric case, the state variables were initialized as fully mobilized in the vertical direction: $h_{11} = -R$ and $c_{11} = -R/2$.

For the CAM model, the state variables p_b and $\boldsymbol{\Omega}$ were initialized as $p_b = p_{\text{ini}}$ and $\boldsymbol{\Omega} = \mathbf{0}$ at $p = p_{\text{ini}}$ for all triaxial tests. For the oedometric test, the deviatoric component of the back stress tensor $\boldsymbol{\Omega}$ has been initialized under such conditions $\Omega_{11} = -0.0001$.

The state variables of the A3-SKH model for triaxial tests were initialized as follows: the pairs (p_b, q_b), (p_a, q_a), and the value of p_0, defining the centre of the yield, history and bounding surfaces, respectively, were assumed to be centered with respect to p_{ini}, i.e. $p_{0,a,b} = 5$ kPa and $q_{a,b} = 0$.

The state variables of the SANICLAY-B model were initialized as follows: the projection center (p_c, $\mathbf{s}_c$) was initialized at the origin of the stress space: $p_c = 0$ and $\mathbf{s}_c = \mathbf{0}$. Initial structuration factor was set to $S_i = 1$ to reflect absence of structure in the tested reconstituted clay. The back-stress ratio tensor $\boldsymbol{\alpha}$ was initialized to $\boldsymbol{\alpha} = \mathbf{0}$. The damage parameter was initialized to $d = 0$.

Acknowledgements The first and fourth authors appreciate the financial support given by the INTER-EXCELLENCE project LTACH19028 by the Czech Ministry of Education, Youth and Sports. The first author appreciates the financial support given by the Charles University Grant Agency (GAUK) with Project Number 200120. The first and fourth authors acknowledge the institutional support by the Center for Geosphere Dynamics (UNCE/SCI/006). The second author gratefully acknowledges the financial support from the German Research Community (DFG, Project: TR 218/27-1).

References

1. Adachi T, Oka F, Hirata T, Hashimoto T, Nagaya J, Mimura M, Pradhan T (1995) Stress-strain behavior and yielding characteristics of eastern osaka clay. Soils Found 35(3):1–13
2. Al Tabbaa A, Wood D (1989) An experimentally based "bubble" model for clay. In: Proceedings of the third international conference on numerical models in geomechanics, pp 91–99, Niagara Falls
3. Azzouz A, Malek M, Baligh A (1989) Cyclic behavior of clays in undrained simple shear. J Geotech Eng 115(5):637–657
4. Benz T (2007) Small-strain stiffness of soils and its numerical consequences. PhD thesis, University of Stuttgart, Germany
5. Benz T, Vermeer P, Schwab R (2009) A small-strain overlay model. Int J Numer Anal Meth Geomech 33(1):25–44
6. Bouckovalas G, Whitman R, Marr W (1984) Permanent displacement of sand with cyclic loading. J Geotech Eng 110(11):1606–1623
7. Boulanger R, Idriss I (2006) Liquefaction susceptibility criteria for silts and clays. J Geotech Geoenviron Eng 132(11):1413–1426
8. Boulanger R, Idriss I (2007) Evaluation of cyclic softening in silts and clays. J Geotech Geoenviron Eng 133(6):641–652
9. Brown S, Lashine A, Hyde A (1975) Repeated load triaxial testing of a silty clay. Géotechnique 25(1):95–114
10. Cai Y, Gu C, Wang J, Juang C (2013) One-way cyclic triaxial behavior of saturated clay: comparison between constant and variable confining pressure. J Geotech Geoenviron Eng 139(5):797–809
11. Dafalias Y, Manzari M, Papadimitriou A (2006) SANICLAY: simple anisotropic clay plasticity model. Int J Numer Anal Meth Geomech 30(12):1231–1257
12. Duque J, Mašín D, Fuentes W (2020) Improvement to the intergranular strain model for larger numbers of repetitive cycles. Acta Geotech 15:3593–3604
13. Duque J, Mašín D, Fuentes W (2021) Hypoplastic model for clays with stiffness anisotropy. In: Proceedings of IACMAG 2021: challenges and innovations in geomechanics, pp 414–421, Turin, Italy,
14. Duque J, Ochmański M, Mašín D, Hong Y, Wang L (2021) On the behavior of monopiles subjected to multiple episodes of cyclic loading and reconsolidation in cohesive soils. Comput Geotech 134:104049
15. Duque J, Yang M, Fuentes W, Mašín D, Taiebat M (2021) Characteristic limitations of advanced plasticity and hypoplasticity models for cyclic loading of sands. Acta Geotech. https://doi.org/10.1007/s11440-021-01418-z
16. Fuentes W, Duque J, Lascarro C (2018) Constitutive simulation of a kaolin clay with vertical and horizontal sedimentation axes. DYNA 85(207):227–235
17. Fuentes W, Gil M, Duque J (2019) Dynamic simulation of the sudden settlement of a mine waste dump under earthquake loading. Int J Min Reclam Environ 33(6):425–443
18. Fuentes W, Mašín D, Duque J (2021) Constitutive model for monotonic and cyclic loading on anisotropic clays. Géotechnique 71(8):657–673
19. Fuentes W, Tafili M, Triantafyllidis T (2017) Constitutive model for clays under the ISA framework. In: Holistic simulation of geotechnical installation processes, benchmarks and simulations, chapter 6, pp 115–129. Springer
20. Fuentes W, Tafili M, Triantafyllidis T (2018) An ISA-plasticity-based model for viscous and non-viscous clays. Acta Geotech 13(3):367–386
21. Fuentes W, Triantafyllidis T (2015) ISA model: a constitutive model for soils with yield surface in the intergranular strain space. Int J Numer Anal Meth Geomech 39(11):1235–1254
22. Fuentes W, Triantafyllidis T, Lascarro C (2017) Evaluating the performance of an ISA-hypoplasticity constitutive model on problems with repetitive loading. In: Holistic simulation of geotechnical installation processes, theoretical results and applications, chapter 16, pp 341–362. Springer
23. Gazibaric I (2017) Untersuchungen zum einfluss des salzgehaltes während der sedimentation auf das materialverhalten von kaolinton unter monotoner und zyklischer belastung. Master Thesis. Karlsruhe Institute of Technology
24. Gotschol A, Kempfert H (2004) Zyklisch viskoelastisch-viskoplastischer stoffansatz nichtbindiger boden und schotter. Bautechnik 81(4):279–285
25. Graham J, Houlsby G (1983) Anisotropic elasticity of a natural clay. Géotechnique 33(2):165–180
26. Gu C, Wang J, Cai Y, Yang Z, Gao Y (2012) Undrained cyclic triaxial behavior of saturated clays under variable confining pressure. Soil Dyn Earthq Eng 40:118–128
27. Gudehus G (1995) Attractors for granular storage and flow. In: Third European symposium – storage and flow of particulate solids, pp 333–345, Nürnberg, Germany
28. Gudehus G (2011) Physical soil mechanics. Springer, Berlin
29. Hyodo M, Hyde A, Yamamoto Y, Fujii T (1999) Cyclic shear strength of undisturbed and remoulded marine clays. Soils Found 39(2):45–58
30. Jerman J, Mašín D (2020) Hypoplastic and viscohypoplastic models for soft clays with strength anisotropy. Int J Numer Anal Meth Geomech 44(10):1396–1416
31. Li X, Dafalias Y (2012) Anisotropic critical state theory: role of fabric. J Eng Mech 138(3):263–275
32. Liao D, Yang Z (2021) Hypoplastic modeling of anisotropic sand behavior accounting for fabric evolution under monotonic and cyclic loading. Acta Geotech 16(7):2003–2029
33. Marr W, Christian J (1981) Permanent displacements due to cyclic wave loading. J Geotech Eng 107(8):1129–1149
34. Mašín D (2014) Clay hypoplasticity model including stiffness anisotropy. Géotechnique 64(3):232–238
35. Mašín D (2019) Modelling of soil behaviour with hypoplasticity: another approach to soil constitutive modelling. Springer, Berlin
36. Mašín D (2021) Triax user's manual, https://soilmodels.com/triax. Charles University, Czech Republic
37. Mašín D, Rott J (2014) Small strain stiffness anisotropy of natural sedimentary clays: review and a model. Acta Geotech 9(2):299–312
38. Ni J, Indraratna B, Geng X, Phillip J (2015) Model of soft soils under cyclic loading. Int J Geomech 15(4):04014067-1–10
39. Niemunis A (2000) Beiträge zum workshop: Boden unter fast zyklischer belastung: Erfahrungen und forschungsergebnisse, veröffentlichungen des institutes für grundbau und bodenmechanik, Ruhr-universität bochum, heft 32
40. Niemunis A (2003) Extended Hypoplastic Models for Soils. Habilitation, Ruhr Universität Bochum, Germany, Heft 34

41. Niemunis A (March 2008) Incremental Driver, user's manual, https://soilmodels.com/idriver. Karlsruhe Institute of Technology, Germany
42. Niemunis A, Grandas C, Prada L (2009) Anisotropic visco-hypoplasticity. Acta Geotech 4(4):293–314
43. Niemunis A, Herle I (1997) Hypoplastic model for cohesionless soils with elastic strain range. Mech Cohesive-Friction Mater 2(4):279–299
44. Niemunis A, Wichtmann T, Triantafyllidis T (2005) A high-cycle accumulation model for sand. Comput Geotech 32(4):245–263
45. Ochmański M, Mašín D, Duque J, Yi H, Lizhong W (2021) Performance of tripod suction bucket foundations for offshore wind turbines: a numerical study. Géotechnique Lett 11(3):230–238
46. Pan K, Xu T, Liao D, Yang Z (2020) Failure mechanisms of sand under asymmetrical cyclic loading conditions: experimental observation and constitutive modelling. Géotechnique, pp 1–14
47. Poblete M, Fuentes W, Triantafyllidis T (2016) On the simulation of multidimensional cyclic loading with intergranular strain. Acta Geotech 11(6):1263–1285
48. Rott J, Mašín D, Boháč J, Krupička M, Mohyla T (2015) Evaluation of K0 in stiff clay by back-analysis of convergence measurements from unsupported cylindrical cavity. Acta Geotech 10(6):719–733
49. Sawicki A, Swidzinski W (1989) Mechanics of a sandy subsoil subjected to cyclic loadings. Int J Numer Anal Methods Geomech 13(5):511–529
50. Schanz T, Vermeer P, Bonnier P (1999) The hardening soil model: formulation and verification. In: Beyond 2000 in computational geotechnics–10 years of Plaxis, pp 281–296, Balkema: Rotterdam
51. Schädlich B, Schweiger H (2013) Influence of anisotropic small strain stiffness on the deformation behavior of geotechnical structures. Int J Geomech 13(6):861–868
52. Seidalinov G (2018) Constitutive and numerical modeling of clay subjected to cyclic loading. PhD thesis, The University of British Columbia, Vancouver
53. Seidalinov G, Taiebat M (2014) Bounding surface SANICLAY plasticity model for cyclic clay behavior. Int J Numer Anal Meth Geomech 38(7):702–724
54. Stallebrass S (1990) Modelling the effect of recent stress history on the behaviour of overconsolidated soils. PhD thesis, City, University of London, United Kingdom
55. Stallebrass S, Taylor R (1997) The development and evaluation of a constitutive model for the prediction of ground movements in overconsolidated clay. Géotechnique 47(2):235–253
56. Tafili M (2019) On the behaviour of cohesive soils: constitutive description and experimental observations. PhD thesis, Institute of Soil Mechanics and Rock Mechanics, Karlsruhe Institute of Technology
57. Tafili M, Fuentes W, Triantafyllidis T (2020) A comparative study of different model families for the constitutive simulation of viscous clays. Int J Numer Anal Meth Geomech 44(5):633–667
58. Tafili M, Grandas C, Wichtmann T, Triantafyllidis T (2021) Constitutive anamnesis model (cam) for fine-grained soils. Int J Numer Anal Methods Geomech (submitted)
59. Tafili M, Triantafyllidis T (2018) On constitutive modelling of anisotropic viscous and non-viscous soft soils. In: 9th European conference on numerical methods in geotechnical engineering, pp 139–147, London
60. Tafili M, Triantafyllidis T (2019) State-dependent dilatancy of soils: experimental evidence and constitutive modeling. In: Triantafyllidis T (ed) Recent developments of soil mechanics and geotechnics in theory and practice, pp 54–84. Springer
61. Tafili M, Triantafyllidis T (2020) AVISA: anisotropic visco-ISA model and its performance at cyclic loading. Acta Geotech 15:2395–2413
62. Tafili M, Triantafyllidis T (2020) Cyclic and monotonic response of silts and clays: experimental analysis and constitutive modelling. Eur J Environ Civ Eng, pp 1–10
63. Tafili M, Triantafyllidis T (2020) A simple hypoplastic model with loading surface accounting for viscous and fabric effects of clays. Int J Numer Anal Methods Geomech 44(2)
64. Tafili M, Wichtmann T, Triantafyllidis T (2021) Experimental investigation and constitutive modeling of the behaviour of highly plastic lower rhine clay under monotonic and cyclic loading. Can Geotech J
65. Taiebat M, Dafalias Y, Peek R (2010) A destructuration theory and its application to SANICLAY model. Int J Numer Anal Meth Geomech 34(10):1009–1040
66. Wichtmann T (2005) Explicit accumulation model for non-cohesive soils under cyclic loading. PhD thesis, Ruhr Universität Bochum, Germany
67. Wichtmann T (2016) Soil behaviour under cyclic loading: experimental observations, constitutive description and applications. Habilitation, Institute of Soil Mechanics and Rock Mechanics, Karlsruhe Institute of Technology
68. Wichtmann T, Triantafyllidis T (2018) Monotonic and cyclic tests on kaolin: a database for the development, calibration and verification of constitutive models for cohesive soils with focus to cyclic loading. Acta Geotech 13(5):1103–1128
69. Yang Z, Liao D, Xu T (2020) A hypoplastic model for granular soils incorporating anisotropic critical state theory. Int J Numer Anal Meth Geomech 44(6):723–748